

PROPERTIES OF THE MOLECULAR CORES OF LOW LUMINOSITY OBJECTS

TIEN-HAO HSIEH^{1,2}, SHIH-PING LAI¹, ARNAUD BELLOCHE², FRIEDRICH WYROWSKI², AND CHAO-LING HUNG^{3,4}¹Institute of Astronomy, National Tsing Hua University (NTHU), Hsinchu 30013, Taiwan²Max-Planck-Institut für Radioastronomie (MPIfR), Bonn, Germany³Institute for Astronomy, University of Hawaii, USA and⁴Harvard-Smithsonian Center for Astrophysics, Cambridge, MA 02138, USA

ABSTRACT

We present a survey toward 16 Low Luminosity Objects (LLOs with an internal luminosity, L_{int} , lower than $0.2 L_{\odot}$) with N_2H^+ (1–0), N_2H^+ (3–2), N_2D^+ (3–2), HCO^+ (3–2) and HCN (3–2) using the Arizona Radio Observatory Kitt Peak 12m Telescope and Submillimeter Telescope. Our goal is to probe the nature of these faint protostars which are believed to be either very low mass or extremely young protostars. We find that the $\text{N}_2\text{D}^+/\text{N}_2\text{H}^+$ column density ratios of LLOs are similar to those of typical starless cores and Class 0 objects. The $\text{N}_2\text{D}^+/\text{N}_2\text{H}^+$ column density ratios are relatively high (> 0.05) for LLOs with kinetic temperatures less than 10 K in our sample. The distribution of N_2H^+ (1–0) line widths spreads between that of starless cores and young Class 0 objects. If we use the line width as a dynamic evolutionary indicator, LLOs are likely young Class 0 protostellar sources. We further use the optically thick tracers, HCO^+ (3–2) and HCN (3–2), to probe the infall signatures of our targets. We derive the asymmetry parameters from both lines and estimate the infall velocities by fitting the HCO^+ (3–2) spectra with two-layer models. As a result, we identify eight infall candidates based on the infall velocities and seven candidates have infall signatures supported by asymmetry parameters from at least one of HCO^+ (3–2) and HCN (3–2).

Subject headings: star: brown dwarfs – stars: low-mass – stars: protostars – ISM: kinematics and dynamics – ISM: molecules – radio lines: ISM

1. INTRODUCTION

Very Low Luminosity Objects (VeLLOs) are embedded protostars with internal luminosity $L_{\text{int}} < 0.1 L_{\odot}$ (Di Francesco et al. 2007). The first VeLLO, L1014-IRS, was identified by Young et al. (2004) toward a dense core previously thought to be starless, L1014. The SED fitting results suggest that L1014-IRS has a very low internal luminosity $\sim 0.09 L_{\odot}$ contributed by the central star and disk (Young et al. 2004; Huard et al. 2006). Three possibilities are proposed to explained VeLLOs' low luminosities (Dunham et al. 2014): they can be 1) very low mass protostars, 2) extremely young protostars, or 3) protostars in a quiescent phase of an episodic accretion process. André et al. (2012) identified a “*pre-brown dwarf*”, Oph-B11, and suggested that brown dwarfs can form in isolated cores as low mass stars (Padoan & Nordlund 2004). By comparing with evolutionary track from models, the low luminosities imply that VeLLOs are substellar sources (current mass $\leq 0.08 M_{\odot}$) embedded in molecular cores (L1014-IRS: Young et al. 2004; Huard et al. 2006, L1521F: Bourke et al. 2006). Lee et al. (2013) suggested that the mass of L328 is at most $0.05 M_{\odot}$ based on the estimate of mass loss rate from outflows. Therefore, VeLLOs could form low mass stars or even brown dwarfs depending on their future accretion. VeLLOs with small mass accretion reservoir (parent cores) are very likely brown dwarfs still in the embedded phase, *i.e.* “*proto brown dwarfs*” (L328: Lee et al. 2009, 2013, L1148: Kauffmann et al. 2011, ICE 348-SMM2E: Palau et al. 2014). Since VeLLOs are usually isolated, they could be brown dwarfs forming through cloud fragmentation followed by gravitational collapse.

On the other hand, VeLLOs' substellar masses also indicate that VeLLOs can be early Class 0 protostars or even younger than Class 0 protostars (IRAM 04191: André et al. 1999; Belloche et al. 2002; Dunham et al. 2006, L1521F: Bourke et al. 2006; Takahashi et al. 2013, Cha-MMS1: Belloche et al. 2006; Tsitali et al. 2013; Väisälä et al. 2014). Considering several age indicators such as T_{bol} and L_{bol} , André et al. (1999) suggested that IRAM 04191 is a young Class 0 object with an age of $\lesssim 3\text{--}5 \times 10^4$ yr. Belloche et al. (2002) later confirmed this by considering the inner free fall region expanding at the sound speed. By studying the outflows, Takahashi et al. (2013) found that L1521F is probably a protostar in the earliest evolutionary stage (age $\lesssim 10^4$ yr). Belloche et al. (2006) found a high level of deuterium fraction and no sign of large scale outflows for the VeLLO Cha-MMS1, suggesting that it has not driven any outflow yet and could be younger than IRAM 04191 and L1521F. The kinematical study in Tsitali et al. (2013) further supports that Cha-MMS1 is either a young Class 0 source or even a first-hydrostatic core (FHSC) (Larson 1969). The FHSC phase represents the short-lived phase during which a hydrostatic compact object forms at the center of a collapsing dense core but has not yet experienced the dissociation of H_2 . (Larson 1969). The dissociation of H_2 at the end of the FHSC phase triggers the second collapse that leads to the formation of the protostar. Several FHSC candidates have been identified but none has been firmly confirmed yet (Cha-MMS1: Belloche et al. 2006, 2011a, L1448-IRS2E: Chen et al. 2010, Per-Bolo 58: Enoch et al. 2010; Dunham et al. 2011, L1451-mm: Pineda et al. 2011, CB17-MMS: Chen et al. 2012, B1-bS, and B1-bN: Pezzuto et al. 2012, Murillo & Lai 2013).

The third possibility – a protostar in a quiescent accretion phase – is possible because the mass accretion can enhance the luminosity of protostars, *i.e.* the accretion luminosity L_{acc} (L673-7: Dunham et al. 2010a, CB130: Kim et al. 2011). Episodic accretion models (Dunham et al. 2010b; Dunham & Vorobyov 2012) have been proposed to interpret the low luminosities of VeLLOs and could be a possible solution of the luminosity problem (Kenyon et al. 1990). The accretion luminosities estimated based on observed CO outflows further support that the accretion process is episodic in low luminosity objects (Dunham et al. 2006, 2010a; Lee et al. 2010). Note that these three possibilities do not conflict with each other; VeLLOs could be a mixture of these three possibilities (Dunham et al. 2014).

The most thorough VeLLO survey has been done by Dunham et al. (2008). The Spitzer Legacy Project “From Molecular Cores to Planet Forming Disks” (c2d; Evans et al. 2003, 2009) mapped five nearby molecular clouds and 95 small dense cores, which provides an excellent opportunity for searching for VeLLOs. Dunham et al. (2008) found a tight relation between the 70 μm flux of protostars and their internal luminosity $L_{\text{int}} = 3.3 \times 10^8 F_{70}^{0.94} L_{\odot}$ based on 1460 synthetic SEDs from the Monte Carlo dust radiative transfer code RADMC (Dullemond & Dominik 2004). Using this relation, Dunham et al. (2008) constructed a list of embedded protostars with low L_{int} and identified 15 VeLLOs from the c2d data. Lately, Hsieh & Lai (2013) developed a new YSO identification method to probe faint YSOs and identified seven additional VeLLO candidates from the c2d survey clouds.

In order to understand the nature of VeLLOs, we focus on probing their evolutionary states using chemical and dynamic evolutionary tracers. It is known that at the center of starless cores, where the temperature is about 10 K and the number density is above 10^4 cm^{-3} , common molecular tracers such as CO and CS freeze out onto dust grain surfaces (Caselli et al. 1999; Tafalla et al. 2002, 2004). Other tracers are required to investigate the dynamical and chemical properties in the cold dense region. The nitrogen-bearing species such as N_2H^+ and NH_3 survive in the gas phase at least for densities in the range of 10^5 – 10^6 cm^{-3} (Crapsi et al. 2005b; Johnstone et al. 2010; Roberts & Millar 2007). Thus, they are important tracers during the prestellar and protostellar phase.

The $\text{N}_2\text{D}^+/\text{N}_2\text{H}^+$ abundance ratio can be an evolutionary indicator in early evolutionary stages of star formation (Crapsi et al. 2005b; Emprechtinger et al. 2009). The $\text{N}_2\text{D}^+/\text{N}_2\text{H}^+$ abundance ratio is affected by the exothermic reaction, $\text{H}_3^+ + \text{HD} \rightleftharpoons \text{H}_2\text{D}^+ + \text{H}_2$, since H_2D^+ transfers the deuteron to N_2 and produces N_2D^+ (Dore et al. 2004). Because CO is a destroyer of H_2D^+ and H_3^+ (Caselli & Ceccarelli 2012), the depletion of CO increases the abundance of H_2D^+ and H_3^+ . The abundance increase of the latter molecule also speeds up the reaction to produce H_2D^+ . As a result, the CO depletion increases the abundance of H_2D^+ as well as N_2D^+ and leads to a high $\text{N}_2\text{D}^+/\text{N}_2\text{H}^+$ abundance ratio in a cold dense region. Crapsi et al. (2005b) found that, in 31 low mass starless cores, the $\text{N}_2\text{D}^+/\text{N}_2\text{H}^+$ column density ratio ($\text{N}(\text{N}_2\text{D}^+)/\text{N}(\text{N}_2\text{H}^+)$ ratio) is correlated with several evolutionary indicators such as core

density, line width and line asymmetry, suggesting that the $\text{N}(\text{N}_2\text{D}^+)/\text{N}(\text{N}_2\text{H}^+)$ ratio increases as a starless core evolves. Emprechtinger et al. (2009) showed that the $\text{N}(\text{N}_2\text{D}^+)/\text{N}(\text{N}_2\text{H}^+)$ ratio decreases as the core evolves while getting hotter and less dense after the central protostar formed. Thus, the $\text{N}(\text{N}_2\text{D}^+)/\text{N}(\text{N}_2\text{H}^+)$ ratio increases in the prestellar core phase and declines in the protostellar core phase (Miettinen & Offner 2013; Huang & Hirano 2013).

Infall motions are also used as an evolutionary indicator since they are likely to occur in the early stages (Emprechtinger et al. 2009). Infall motions in protostars can be traced with observations including both optically thin and thick lines. For a protostar with an envelope dominated by infall, the foreground gas and background gas are red-shifted and blue shifted, respectively, with respect to the systemic velocity. If the foreground gas is colder than the central region, the red-shifted emission of an optically thick line can be absorbed, resulting in a spectral line asymmetry with a blue-shifted peak (Mardones et al. 1997).

We study the chemical and physical properties of 16 Low Luminosity Objects (LLOs, $L_{\text{int}} \leq 0.2 L_{\odot}$) from Dunham et al. (2008). We describe our sample and observations in §2 and report the results in §3. The data analysis is presented in §4 and the properties of LLOs are discussed in §5. We summarize the results in §6.

2. OBSERVATIONS

2.1. Sample

Using the c2d data (Evans et al. 2003, 2009), Dunham et al. (2008) identified 50 embedded protostars with $L_{\text{int}} \leq 1 L_{\odot}$ and 15 sources out of them are VeLLOs ($L_{\text{int}} \leq 0.1 L_{\odot}$). Hereafter we use the combination of the first letter of the three authors’ last names plus the source number in their paper as our source name (*e.g.* DCE 185). Our sample consists of 10 VeLLOs out of the 15 sources. We excluded five sources: 1) DCE145 was identified as a background galaxy based on our CFHT Ks band (2.146 μm) outflow survey (Hsieh & Lai in preparation), 2) DCE 161 and DCE 018 are unobservable using telescopes at the Arizona Radio Observatory (ARO), and 3) DCE 024 (CB-130) and DCE 032 (L1148) have spectra contaminated by their reference positions that were by mistake set too close to the sources. In order to reduce the bias from the small sample, we added 6 Low Luminosity Objects (LLOs, $0.1 L_{\odot} < L_{\text{int}} \leq 0.2 L_{\odot}$) located in the two closest molecular clouds, Ophiuchus (125 pc) and Perseus (250 pc) from the Dunham et al. (2008) sample. This sample includes 10 Class 0 sources and 6 Class I sources (bolometric temperature $T_{\text{bol}} > 70$ K, Chen et al. 1995) as shown in Table 1. These sources show evidence that they are indeed embedded, allowing us to study the chemical and physical properties of their parent cores.

2.2. Kitt Peak 12m Telescope observations

We observed N_2H^+ (1–0) toward the 16 LLOs in November 2012 and February 2013 using the Kitt Peak 12 meter Telescope (KP12m) at the Arizona Radio Observatory (ARO). We used the position-switching mode pointed toward the infrared sources (Dunham et al. 2008) (Table 1). The integration time (including on and

TABLE 1
LLO SAMPLE

Source number	Other name	R.A. (J2000.0)	Dec (J2000.0)	L_{int} L_{\odot}	Distance (pc)	T_{bol} (K)
DCE 065		03:28:39.1	31:06:01.8	0.02	250 (50)	29 (3)
DCE 004	L1521F	04:28:38.9	26:51:35.6	0.03	140 (10)	20 (3)
DCE 064		03:28:32.6	31:11:05.3	0.03	250 (50)	65 (12)
DCE 031	L673-7	19:21:34.8	11:21:23.4	0.04	300 (100)	24 (6)
DCE 001	IRAM 04191	04:21:56.9	15:29:46.0	0.04	140 (10)	27 (3)
DCE181		16:28:48.5	-24:28:38.6	0.05	125 (25)	430 (19)
DCE 081		03:30:32.7	30:26:26.5	0.06	250 (50)	33 (4)
DCE 025	L328	18:16:59.5	-18:02:30.5	0.07	270 (50)	62 (9)
DCE 038	L1014	21:24:07.6	49:59:08.9	0.09	250 (50)	66 (21)
DCE 185	IRAS 16253-2429	16:28:21.6	-24:34:23.4	0.09	125 (25)	30 (2)
DCE 109		03:44:21.4	31:59:32.6	0.11	250 (50)	345 (4)
DCE 092		03:33:14.4	31:07:10.9	0.14	250 (50)	47 (5)
DCE 182		16:27:05.2	-24:36:29.5	0.15	125 (25)	105 (2)
DCE 107		03:44:02.4	32:02:04.9	0.15	250 (50)	76 (4)
DCE 063		03:27:38.3	30:13:58.8	0.20	250 (50)	199 (3)
DCE 090		03:32:29.2	31:02:40.9	0.20	250 (50)	114 (17)

NOTE. — The source informations, Col. (3)-(7), are from Dunham et al. (2008). The order of sources is based on their internal luminosities (Col. (5)) and is used in this paper.

off positions) for each source was 5–15 min. The rms noise levels are in a range of 0.06 to 0.13 K at a spectral resolution of 0.078 km s⁻¹. The half power beam width (*HPBW*) is $\sim 67.5''$ and the pointing accuracy is 5'' rms. The spectra were calibrated in main-beam temperature scale assuming a main-beam efficiency of 0.59 \pm 0.07 based on the Saturn measurement (see ARO web page¹). We used the 3mm (ALMA Type Band 3) receiver and the backend Millimeter Autocorrelator with 6.2 kHz spectral resolution (~ 0.019 km s⁻¹), but the spectra were smoothed to 0.078 km s⁻¹ for the analysis.

2.3. SMT observations

The N₂H⁺ (3–2), N₂D⁺ (3–2), HCO⁺ (3–2) and HCN⁺ (3–2) observations were carried out between November 2012 and February 2014 using the Submillimeter Telescope (SMT) at the ARO, except for N₂D⁺ (3–2) observation for DCE 065 which was carried out in December 2009. The pointed positions were centered at the infrared sources (Table 1) and the observations were performed with the position-switching mode. The integration time was 6–24 min for N₂H⁺ (3–2), 30–42 min for N₂D⁺ (3–2), 6 min for HCO⁺ (3–2) and 5 min for HCN (3–2) for each source. The rms noise levels are 0.02–0.09 K for N₂H⁺ (3–2), 0.01–0.04 K for N₂D⁺ (3–2), 0.04–0.13 K for HCO⁺ (3–2), and 0.05–0.08 K for HCN (3–2) at a spectral resolution of 250 kHz. The *HPBW*s are 27'' for N₂H⁺ (3–2), 32.6'' for N₂D⁺ (3–2) and $\sim 26''$ for both HCO⁺ (3–2) and HCN (3–2), and the pointing accuracy is 1'' rms. We used the ALMA Type 1.3mm receiver and the filter-bank backend. The main beam efficiency is 0.74 for all lines². The spectral resolution is 250 kHz corresponding to 0.27 km s⁻¹ for N₂H⁺ (3–2), 0.32 km s⁻¹ for N₂D⁺ (3–2) and ~ 0.28 km s⁻¹ for both HCO⁺ (3–2) and HCN (3–2).

3. RESULTS

All the data were reduced using the CLASS program³. Figure 1 shows the spectra of N₂H⁺ (1–0), N₂H⁺ (3–2), N₂D⁺ (3–2), HCO⁺ (3–2) and HCN (3–2) for our targets.

3.1. N₂H⁺ and N₂D⁺

3.1.1. Spectra

The N₂H⁺ (1–0) lines were detected in all our targets although some sources have very weak detections. We fitted all hyperfine components in N₂H⁺ (1–0) by considering their relative intensities using our own code. The code considers the relative intensities of all components similar to the fitting function “METHOD HFS” in CLASS. The only difference is that we fit the excitation temperature (T_{ex}) directly which gives us a direct estimate of its uncertainty whereas the uncertainty on T_{ex} needs to be obtained through error propagation from two parameters when using CLASS. Since the “METHOD HFS” does not provide the covariance of the output parameters, our fitting process provides a more accurate error estimate for T_{ex} . Table 2 lists the best fitting results including systemic velocities (V_{LSR}), line widths (ΔV), optical depths (τ) and excitation temperatures (T_{ex}), together with integrated intensities (W).

The N₂H⁺ (3–2) lines were detected toward all the targets except DCE 181 and DCE 182 which have weak detections in N₂H⁺ (1–0). The N₂D⁺ (3–2) lines were detected toward 11 targets and were undetected in DCE 181, 025, 038, 182 and 090. The satellite lines are not clearly detected with the rms noise σ of 0.02–0.09 K for N₂H⁺ (3–2) and 0.01–0.04 K for N₂D⁺ (3–2). This prevents us from deriving the excitation temperatures and optical depths (for most of our targets) with HFS fitting. However, we can estimate the upper limits of τ for each source. If we use a threshold 3 σ as the upper limit of the undetected satellite lines, we obtain a corresponding upper limit of τ . (The optical depths of N₂H⁺ (3–2) of DCE 065, 81 and 092 are derived by fitting the hyperfine structure with relative intensity.) We thus list the integrated intensities and upper limits of optical depths for N₂D⁺ and N₂H⁺ (3–2) in Table 2.

¹ http://aro.as.arizona.edu/12_obs_manual/appendix_C.htm

² http://aro.as.arizona.edu/smt_docs/smt_beam_eff.htm

³ <http://www.iram.fr/IRAMFR/GILDAS/>

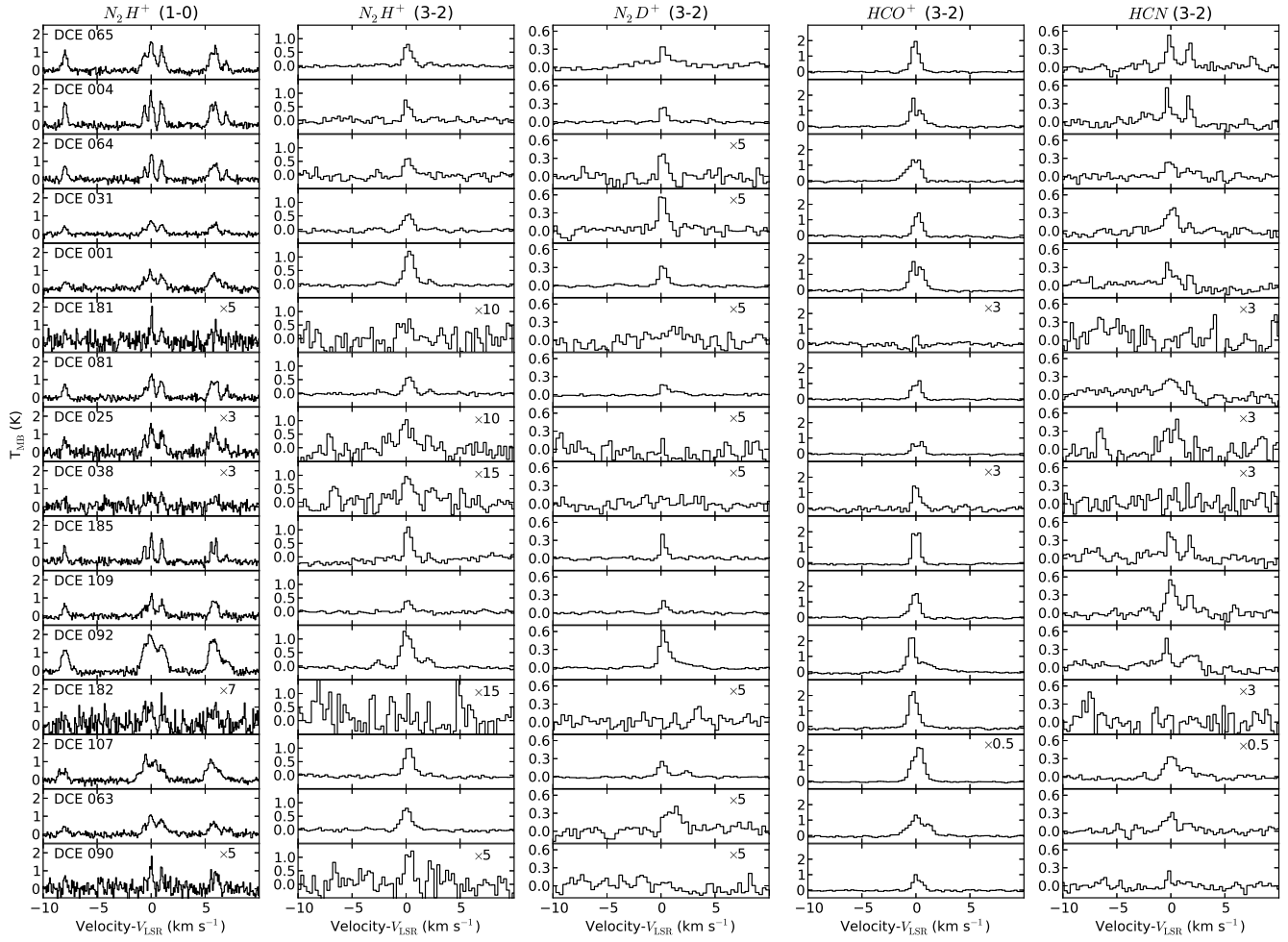


FIG. 1.— The spectra of N_2H^+ (1-0), N_2H^+ (3-2), N_2D^+ (3-2), HCO^+ (3-2) and HCN (3-2) for all our LLO targets. The velocities are shifted by the V_{LSR} which is from the N_2H^+ (1-0) hyperfine fitting (Table 2). The spectra of sources with weak or no detections are multiplied by a factor labeled in the upper right corner.

3.1.2. Two components of DCE 107

The N_2H^+ (1-0) spectrum of DCE 107 shows a clear double peak structure. The SCUBA 850 μm continuum emission image from the COMPLETE project (Ridge et al. 2006) has resolved two components with a separation of $\sim 35''$ within our observing beam. Therefore, we suspect that the two velocity components seen in the N_2H^+ (1-0) spectrum correspond to the two continuum sources in the 850 μm image (hereafter DCE 107a and DCE 107b). We fitted the spectrum using a superposition of two sets of hyperfine components; each set has its own systemic velocity, line width, optical depth and excitation temperature (Table 2). The fitting result seems to be reasonable by comparing with the N_2H^+ (1-0) observations from Kirk et al. (2007). Using the IRAM 30m telescope ($\theta_{FWHM} \sim 27''$), Kirk et al. (2007) observed DCE 107 (core 21 in their paper) at a position $\sim 12''$ away from our position (the infrared source) and $\sim 8''$ away from DCE107a. They detected only one velocity component, supporting our interpretation above, and they obtained a line width of $0.65 \pm 0.009 \text{ km s}^{-1}$ and a systemic velocity of $9.02 \pm 0.008 \text{ km s}^{-1}$ which are very close to the values we derive for DCE 107a ($\Delta V = 0.61 \pm 0.06 \text{ km s}^{-1}$ and $V_{LSR} = 8.95 \pm 0.02 \text{ km s}^{-1}$).

3.2. HCO^+ and HCN observations

3.2.1. spectra

The HCO^+ (3-2) line was detected toward all 16 LLO targets and the HCN (3-2) line toward 13 out of the 16 targets (undetected in DCE 181, 038 and 182). We use HCO^+ (3-2) and HCN (3-2) as our optically thick tracers to search for infall signatures. The optical depth of HCN (3-2) was estimated by fitting the hyperfine components. The optical depths of our targets are all larger than 5 (except for DCE 025 and DCE 090 which have very uncertain values), indicating that the HCN (3-2) lines are optically thick toward our targets (Table 3). This feature can be easily seen in the spectra since the satellite lines ($F=3 \rightarrow 3$) are significant compared with the main components. Note that the satellites $F=2 \rightarrow 2$ are much weaker or undetected although $F=2 \rightarrow 2$ and $F=3 \rightarrow 3$ have equal line strengths (anomalies, Daniel et al. 2006).

4. ANALYSIS

4.1. N_2H^+ Non-LTE RADEX analysis

We used the non-LTE radiative transfer code RADEX (van der Tak et al. 2007) to model the N_2H^+ (1-0) and (3-2) spectra for our targets. The densities of low mass

TABLE 2
LINE PROPERTIES

Source	$\text{N}_2\text{H}^+ (1-0)$					$\text{N}_2\text{H}^+ (3-2)$		$\text{N}_2\text{D}^+ (3-2)$	
	$W_{\text{N}_2\text{H}^+_{J=1-0}}$ [K km s ⁻¹]	V_{LSR} [km s ⁻¹]	ΔV (FWHM) [km s ⁻¹]	$\tau_{\text{tot}}^{\text{a}}$	T_{ex}^{b} [K]	$W_{\text{N}_2\text{H}^+_{J=3-2}}$ [K km s ⁻¹]	$\tau_{\text{tot}}^{\text{c}}$	$W_{\text{N}_2\text{D}^+_{J=3-2}}$ [K km s ⁻¹]	$\tau_{\text{tot}}^{\text{c}}$
DCE 065	3.58 (0.07)	7.02 (0.01)	0.46 (0.02)	5.00 (1.13)	4.95 (0.30)	0.69 (0.04)	2.84 (1.10)	0.34 (0.04)	<13.10
DCE 004	3.19 (0.08)	6.44 (0.01)	0.29 (0.01)	14.05 (2.22)	4.34 (0.09)	0.52 (0.06)	<12.30	0.19 (0.02)	<6.60
DCE 064	2.31 (0.08)	7.19 (0.01)	0.35 (0.02)	2.94 (1.27)	5.52 (0.87)	0.56 (0.06)	<18.70	0.06 (0.02)	<19.90
DCE 031	1.62 (0.08)	7.15 (0.01)	0.51 (0.03)	2.07 (1.30)	4.60 (0.91)	0.55 (0.04)	<8.20	0.11 (0.01)	<14.00
DCE 001	2.28 (0.07)	6.63 (0.02)	0.62 (0.04)	3.05 (1.49)	4.39 (0.56)	1.29 (0.03)	<2.40	0.29 (0.01)	<4.10
DCE 181	0.33 (0.06)	3.67 (0.01)	0.26 (0.03)	0.10 (0.07)	14.48 (18.46)	<0.02 ^d	-	<0.02 ^d	-
DCE 081	2.62 (0.07)	6.05 (0.01)	0.40 (0.02)	5.79 (1.44)	4.43 (0.24)	0.56 (0.03)	8.68 (2.28)	0.14 (0.01)	<7.30
DCE 025	0.95 (0.07)	6.61 (0.01)	0.40 (0.03)	4.43 (2.12)	3.51 (0.24)	0.11 (0.02)	<19.90	<0.02 ^d	-
DCE 038	0.40 (0.05)	4.24 (0.03)	0.44 (0.07)	1.95 (4.19)	3.40 (1.16)	0.07 (0.02)	<19.90	<0.03 ^d	-
DCE 185	2.10 (0.05)	4.04 (0.004)	0.23 (0.01)	5.76 (1.51)	4.93 (0.34)	0.73 (0.03)	<19.50	0.21 (0.01)	<4.90
DCE 109	2.07 (0.07)	9.12 (0.01)	0.45 (0.02)	0.87 (1.31)	8.49 (7.59)	0.32 (0.04)	<12.10	0.14 (0.02)	<7.50
DCE 092	6.46 (0.08)	6.27 (0.01)	0.66 (0.02)	6.89 (0.88)	5.12 (0.14)	1.48 (0.05)	5.06 (1.33)	0.59 (0.02)	<0.90
DCE 182	0.32 (0.05)	4.84 (0.03)	0.37 (0.07)	5.55 (6.20)	2.97 (0.16)	<0.03 ^d	-	<0.02 ^d	-
DCE 107a	1.34 (0.85)	8.95 (0.02)	0.62 (0.06)	1.57 (0.46)	4.61 (0.76)	1.04 (0.04)	<3.90	0.23 (0.02)	<4.50
DCE 107b	0.87 (1.66)	8.40 (0.01)	0.33 (0.03)	1.08 (0.87)	6.30 (4.45)	1.04 (0.04)	<3.90	0.23 (0.02)	<4.50
DCE 063	2.59 (0.08)	4.71 (0.02)	0.65 (0.04)	1.35 (1.31)	5.92 (2.53)	0.84 (0.04)	<4.50	0.13 (0.02)	<19.90
DCE 090	0.37 (0.04)	6.62 (0.01)	0.29 (0.03)	0.10 (1.79)	15.15 (325.44)	0.21 (0.03)	<19.90	<0.02 ^d	-

NOTE. — The values in parenthesis represent 1σ uncertainties.

^a τ represents the total opacity which is the sum of the optical depth of all hyperfine components. The fitting limitation of τ is set to be $\tau > 0.1$.

^b The excitation temperatures are computed by assuming a beam filling factor of 1.

^c The upper limits of the total opacity τ are estimated based on the peak intensities and the rms noise levels since most of the satellite lines are undetected.

^d The integrated intensity upper limits is estimated using a peak temperature detection limit of 3σ , and assuming the line width is the same as $\text{N}_2\text{H}^+ (1-0)$.

TABLE 3
LINE PROPERTIES OF $\text{HCO}^+ (3-2)$ AND $\text{HCN} (3-2)$

Source	$\text{HCO}^+ (3-2)$		$\text{HCN} (3-2)$			
	$W_{\text{HCO}^+_{J=3-2}}$ [K km s ⁻¹]	V_{LSR} [km s ⁻¹]	ΔV [km s ⁻¹]	$\tau_{\text{tot}}^{\text{b}}$	T_{ex}^{c} [K]	$W_{\text{HCN}_{J=3-2}}$ [K km s ⁻¹]
DCE 065	5.96 (0.03)	6.92 (0.01)	0.27 (0.03)	28.04 (9.85)	3.98 (0.10)	2.37 (0.04)
DCE 004	6.52 (0.07)	6.30 (0.02)	0.37 (0.04)	43.28 (18.33)	3.75 (0.09)	1.99 (0.07)
DCE 064	7.25 (0.05)	7.05 (0.05)	0.47 (0.09)	13.19 (7.46)	3.50 (0.09)	1.43 (0.06)
DCE 031	4.37 (0.05)	7.17 (0.05)	0.72 (0.13)	5.16 (3.04)	3.82 (0.11)	1.81 (0.07)
DCE 001	8.23 (0.07)	6.66 (0.05)	0.56 (0.07)	19.64 (8.84)	3.54 (0.08)	1.50 (0.07)
DCE 181	0.19 (0.02)	-	-	-	-	-
DCE 081	4.00 (0.04)	6.01 (0.05)	0.57 (0.07)	29.90 (13.24)	3.54 (0.09)	1.83 (0.05)
DCE 025	2.93 (0.04)	6.71 (0.21)	1.30 (1.05)	1.21 (7.07)	3.34 (1.68)	0.60 (0.06)
DCE 038	1.36 (0.03)	-	-	-	-	-
DCE 185	6.10 (0.07)	4.05 (0.03)	0.32 (0.05)	36.18 (15.39)	3.87 (0.10)	2.01 (0.09)
DCE 109	5.63 (0.03)	9.13 (0.03)	0.54 (0.05)	17.57 (5.14)	3.97 (0.08)	2.73 (0.04)
DCE 092	10.06 (0.10)	5.82 (0.04)	0.44 (0.07)	12.74 (6.40)	3.76 (0.10)	2.36 (0.11)
DCE 182	7.63 (0.06)	-	-	-	-	-
DCE 107	19.73 (0.07)	8.91 (0.03)	0.73 (0.06)	8.20 (2.29)	4.37 (0.07)	4.38 (0.10)
DCE 063	8.18 (0.05)	4.45 (0.05)	0.67 (0.08)	14.09 (5.77)	3.51 (0.07)	1.73 (0.05)
DCE 090	3.03 (0.04)	6.42 (0.19)	0.29 (0.55)	0.10 (3.50)	9.32 (174.78)	0.67 (0.04)

NOTE. — The values in parenthesis represent 1σ uncertainties.

^a τ represents the total opacity which is the sum of the optical depth of all hyperfine components. The fitting limitation of τ is set to be $\tau > 0.1$.

^b The excitation temperatures are computed by assuming a beam filling factor of 1.

protostellar cores can be lower than the critical densities of $\text{N}_2\text{H}^+ (1-0)$ and $(3-2)$. This means that the local thermal equilibrium (LTE) assumption is not appropriate for deriving the true physical properties. RADEX provides fast non-LTE analysis for molecular line spectra in a uniform medium, which involves collisional and radiative processes. The N_2H^+ line data (energy levels, statistical weights, Einstein A-coefficients and collisional rate coefficients) are from Daniel et al. (2005) and Schöier et al. (2005), and were taken from the Lei-

den Atomic and Molecular Database (LAMDA).

We used RADEX to derive the cores' kinetic temperatures (T_{kin}), N_2H^+ column densities ($N(\text{N}_2\text{H}^+)$), H_2 densities (n_{H_2}) and source sizes. The former three parameters are related to the cores' evolutionary state and/or may decide the mass of stars formed in the future. The core sizes, together with the beam sizes, yield the beam filling factors that determine the scale of the spectra. Since the beam sizes of our $\text{N}_2\text{H}^+ (1-0)$ and $(3-2)$ observations are different, the beam filling factors affect the

intensity ratios of N_2H^+ (1–0)/(3–2) as well as our derived physical parameters.

We constructed a model grid for each source to derive the physical parameters. The grid is composed with three variances, kinetic temperature, N_2H^+ column density and H_2 density, while the line width is fixed to that from the hyperfine fitting. The step sizes of the grid are 0.5 K for T_{kin} , 0.025 and 0.05 in decimal log scale for $\text{N}(\text{N}_2\text{H}^+)$ and n_{H_2} , respectively. Each cell in the grid contains the synthetic spectra of N_2H^+ (1–0) and (3–2). The synthetic spectra are built-up based on RADEX results which include the excitation temperatures (T_{ex}) and optical depths (τ) for all hyperfine components. The spectra are constructed using the equation

$$T_{\text{MB}}(v) = \Psi \left(\frac{\sum J(T_{\text{ex}}^i) \tau_i(v)}{\sum \tau_i(v)} - J(T_{\text{bg}}) \right) (1 - \exp(-\sum \tau_i(v))), \quad (1)$$

where Ψ is the beam filling factor, T_{bg} is the cosmic background temperature (2.73 K), and $J(T) = [h\nu/k]/[\exp(h\nu/kT) - 1]$. To approach a reasonable intensity at the hyperfine component overlapping region, we used a weighting emissivity term, $\frac{\sum J(T_{\text{ex}}^i) \tau_i(v)}{\sum \tau_i(v)}$. This conception is similar to the averaged excitation temperature in Daniel et al. (2006) for discussing the line anomalies (*i.e.* T_{ex} are different between the hyperfine components.). The weighting is based on the optical depths contributed from all components at a specific velocity. $\sum \tau_i(v)$ is the superposition of optical depths contributed from all components at such velocity. Note that RADEX does not consider the line overlap, which may make our approach uncertain at such regions (Daniel et al. 2006; van der Tak et al. 2007). The beam filling factor (*i.e.* source size) is the free parameter determining the scale of the synthetic spectra. As a result, we obtained a χ^2 distribution (see Appendix and Figure A1) and the corresponding best fitting core size distribution in the grid for each source. Figure A2 shows an example (DCE 081) of the best fitting results using our RADEX synthetic spectra compared with using HFS fitting. The RADEX synthetic spectra seem to fit the hyperfine anomalies better than HFS fitting for the 121-011 and 122-011 components. For the 112-012 component, both fitting processes can not fit the anomalies well. For most of our sources, no significant difference is found between the two fitting processes. The best fitting results are listed in Table 4 for the 13 targets with both N_2H^+ (1–0) and (3–2) detections and only one velocity component. The errors are defined with a 68.3% confidence level area (Press et al. 1992) for four free parameters (T_{kin} , $\text{N}(\text{N}_2\text{H}^+)$, n_{H_2} and core sizes).

Out of the 13 targets, T_{kin} and n_{H_2} are constrained in 5 sources but not in 8 sources (which have a confidence interval exceeding the boundary of our model grid, see Figure A1). For the 5 sources with constraints, the average error is ~ 3.1 K for T_{kin} and a multiplicative factor of ~ 0.36 for n_{H_2} (steps by log scale). DCE 064 has the most uncertain T_{kin} which is $13.5^{+8.0}_{-5.5}$ K and DCE 065 has the most uncertain n_{H_2} which is $10^{6.1^{+0.6}_{-0.4}} \text{ cm}^{-3}$. For the 8 unconstrained sources, we list the parameters from the best-fit model and upper or lower limits of these parameters (Table 4).

TABLE 4
RADEX FITTING RESULTS

Source	T_{kin} [K]	n_{H_2} $\log_{10} [\text{cm}^{-3}]$	$\text{N}(\text{N}_2\text{H}^+)$ $\log_{10} [\text{cm}^{-2}]$	FWHM [arcsec]
DCE065	$7.5^{+2.5}_{-1.5}$	$6.1^{+0.6}_{-0.4}$	$13.10^{+0.07}_{-0.12}$	58^{+27}_{-12}
DCE004	$8.0^{+3.5}_{-\infty}$	$5.8^{+0.4}_{-0.4}$	$13.35^{+0.15}_{-0.30}$	45^{+66}_{-9}
DCE064	$13.5^{+8.0}_{-5.5}$	$5.4^{+0.6}_{-0.3}$	$13.02^{+0.18}_{-0.24}$	42^{+25}_{-8}
DCE031	$25.5^{+\infty}_{-13.0}$	$5.0^{+0.5}_{-\infty}$	$13.23^{+0.14}_{-0.21}$	27^{+7}_{-4}
DCE001	$6.5^{+1.0}_{-0.0}$	$7.3^{+0.2}_{-0.7}$	$13.17^{+0.06}_{-0.07}$	42^{+3}_{-3}
DCE081	$16.5^{+6.0}_{-5.5}$	$5.2^{+0.3}_{-0.2}$	$13.32^{+0.13}_{-0.09}$	34^{+4}_{-3}
DCE025	$6.0^{+9.0}_{-\infty}$	$5.6^{+\infty}_{-1.0}$	$12.82^{+0.31}_{-0.62}$	$40^{+\infty}_{-11}$
DCE038	$9.0^{+\infty}_{-3.0}$	$5.0^{+\infty}_{-\infty}$	$12.95^{+0.55}_{-1.35}$	$24^{+\infty}_{-9}$
DCE185	$6.5^{+3.0}_{-\infty}$	$7.3^{+\infty}_{-1.3}$	$12.78^{+0.22}_{-0.13}$	77^{+18}_{-34}
DCE109	$7.5^{+15.5}_{-\infty}$	$6.0^{+\infty}_{-1.0}$	$12.63^{+0.35}_{-0.31}$	$85^{+\infty}_{-40}$
DCE092	$7.5^{+0.5}_{-0.5}$	$6.3^{+0.2}_{-0.1}$	$13.37^{+0.06}_{-0.02}$	65^{+7}_{-7}
DCE063	$33.0^{+25.5}_{-25.5}$	$5.0^{+1.4}_{-\infty}$	$13.23^{+0.09}_{-0.33}$	35^{+19}_{-4}
DCE090	$30.5^{+\infty}_{-21.0}$	$5.2^{+0.8}_{-\infty}$	$13.28^{+0.29}_{-0.40}$	11^{+6}_{-3}

NOTE. — The parameters of the best-fit model are listed in the table. The errors presented here are with 68.3% confidence level. The ∞ error indicates that the parameter is not constrained at the upper or lower end.

We here compare the H_2 densities of our fitting results with the literature for several well-studied objects. Our derived densities are quite consistent with that of DCE 004 (L1521F) and 038 (L1014) in Crapsi et al. (2004, 2005a). Considering the 1.2 mm continuum maps and a density profile, $n_{\text{H}_2} = n_0/(1+r/r_0)^\alpha$, they found $n_0 = 10^6 \text{ cm}^{-3}$ and $\alpha \sim 2$ for DCE 004, and $n_0 = 2.5 \times 10^5 \text{ cm}^{-3}$ and $\alpha \sim 2.7$ for DCE 038 (both with a “flat” region, $r_0 \sim 20''$). Our derived densities ($6.3 \times 10^5 \text{ cm}^{-3}$ within $r < 23''$ for DCE 004, and 10^5 cm^{-3} within $r < 12''$ for DCE 038) are very close to the results from the literature (but DCE 038 is not well constrained in our sample). However, the particularly high densities of DCE 001 (IRAM 04191) and DCE 185 (IRAS 16253) are very likely overestimated. For DCE 001, Belloche et al. (2002) derived a density of $\sim 2 \times 10^5 \text{ cm}^{-3}$ at a radius of $20''$, based on the dust continuum emission and the radiative transfer modeling of CS transitions. Our estimated density, $2 \times 10^7 \text{ cm}^{-3}$ within a radius of $\sim 21''$ is obviously too high. DCE 001 has the highest N_2H^+ (3–2)/(1–0) intensity ratio among our targets (Table 2). In addition, our observed N_2H^+ (1–0) peak intensity is lower than that from the IRAM 30m telescope (Belloche et al. 2002) by a factor of ~ 3 . The optical depth derived from the HFS fitting is also lower than that in Belloche et al. (2002) by a factor of ~ 2 . We therefore speculate that our observation with a large beam ($HPBW = 67.5''$) is seriously contaminated by diffuse regions whereas the IRAM 30m observation ($HPBW \sim 27''$) is not. Our N_2H^+ (3–2) observations have the same angular resolution as the IRAM 30m observations of N_2H^+ (1–0), so they likely trace the same region. The contamination of our N_2H^+ (1–0) data by more diffuse material likely leads to an overestimate of the N_2H^+ (3–2)/(1–0) intensity ratio that is used in our analysis to derive constraints on the density. Taking into account beam filling factor effects as we did in our analysis cannot solve this problem. The case of DCE 185 is very similar. The high N_2H^+ (3–2)/(1–0) intensity ratio is likely due to the contamination of our 1-0 spectrum by more diffuse regions; the high density ($2 \times$

10^7 cm^{-3}) within a radius of $39''$ are unlikely to be true since the envelope mass of DCE 185 is small ($0.15\text{--}1.0 M_\odot$; Barsony et al. 2010, Stanke et al. 2006, Enoch et al. 2008 and Tobin et al. 2012). Some sources with high N_2H^+ (3–2)/(1–0) intensity ratios may also suffer from this problem such as DCE 031 and 063 (intensity ratios ~ 3). As a result, these two sources have the highest kinetic temperatures among our targets for explaining their high intensity ratios in our RADEX fittings. The kinetic temperatures could thus be overestimated. It is likely that sources with relatively low N_2H^+ (3–2)/(1–0) intensity ratios (and/or high opacities) are less affected by the contamination of diffuse regions. N_2H^+ (3–2) and (1–0) observations with a similar beam size are required for deriving the densities of DCE 001, 185, 031, and 063 in a more reliable way.

4.2. $\text{N}_2\text{D}^+/\text{N}_2\text{H}^+$ column density ratio

The N_2D^+ column density is difficult to derive with only the $J = 3 \rightarrow 2$ transition because we cannot derive the excitation temperature (T_{ex}) and optical depth (τ) which are crucial for determining the column density (see §3.1.1). In addition, the excitation temperatures could be very different between different transitions under non-LTE conditions (see Fig. 17 in Daniel et al. 2007). Using N_2H^+ as an example, the excitation temperatures of N_2H^+ (3–2) are lower than that of N_2H^+ (1–0) by 0.3 – 4 K in our RADEX best-fit models (see §4.1).

With only one transition, we have to perform an LTE analysis to derive the column density of N_2D^+ . However, a reasonable $\text{N}_2\text{D}^+/\text{N}_2\text{H}^+$ column density ratio ($\text{N}(\text{N}_2\text{D}^+)/\text{N}(\text{N}_2\text{H}^+)$) can still be obtained considering that Daniel et al. (2007) found very similar excitation temperatures for N_2D^+ and N_2H^+ in a given transition ($J = 1 \rightarrow 0$ or $J = 2 \rightarrow 1$ or $J = 3 \rightarrow 2$, see their Fig. 17). For the $J = 3 \rightarrow 2$ transition, the largest difference in excitation temperature is $\lesssim 0.5$ K at a H_2 density of $\sim 10^5 \text{ cm}^{-3}$. We therefore assume that the $\text{N}(\text{N}_2\text{D}^+)/\text{N}(\text{N}_2\text{H}^+)$ ratio derived using the same transition ($J = 3 \rightarrow 2$) in both molecules will be very close to the actual ratio, even when deriving each column density with LTE equations. We use the excitation temperatures of N_2H^+ (3–2) obtained from the RADEX best-fit model for both N_2H^+ and N_2D^+ (3–2). (Since each hyperfine component of N_2H^+ (3–2) has a different T_{ex} , we use the averaged excitation temperature as defined in Daniel et al. (2006), $T_{\text{ave}} = \frac{h\nu}{k} / \ln[1 + \frac{h\nu}{k} \sum \frac{\tau_i}{T_{\text{ex}}^i}]$.) The opacity of N_2D^+ (3–2) is then calculated by fitting the hyperfine components with T_{ex} fixed to the value derived for N_2H^+ (3–2). Note the N_2D^+ (3–2) spectra were scaled with the beam filling factors derived from source sizes. The column densities are derived using Eq. (76) in Mangum & Shirley (2013) and equation A4 in Caselli et al. (2002),

$$N_{\text{tot}}^{\text{thick}} = N_{\text{tot}}^{\text{thin}} \frac{\tau}{1 - \exp(-\tau)} \quad (2)$$

TABLE 5
 $\text{N}_2\text{D}^+/\text{N}_2\text{H}^+$ COLUMN DENSITY RATIOS

Source	$\text{N}(\text{N}_2\text{H}^+)$ 10^{12} cm^{-2}	$\text{N}(\text{N}_2\text{H}^+)$ 10^{12} cm^{-2}	$\text{N}(\text{N}_2\text{D}^+)$ 10^{11} cm^{-2}	$\text{N}(\text{N}_2\text{D}^+)/\text{N}(\text{N}_2\text{H}^+)$
DCE 065	16.73 (0.96)	27.54 (1.39)	23.91 (2.81)	0.087 (0.011)
DCE 004	33.94 (2.24)	88.26 (10.88)	23.96 (2.92)	0.027 (0.005)
DCE 064	14.15 (1.69)	27.95 (3.20)	5.03 (1.46)	0.018 (0.006)
DCE 031	21.38 (3.38)	28.53 (2.18)	11.43 (1.63)	0.040 (0.006)
DCE 001	8.53 (1.41)	24.96 (0.54)	13.97 (0.40)	0.056 (0.002)
DCE 081	28.96 (2.43)	54.71 (0.27)	15.50 (0.82)	0.028 (0.002)
DCE 025	6.02 (1.85)	14.04 (2.76)	-	-
DCE 185	6.72 (0.48)	11.83 (0.48)	7.55 (0.46)	0.064 (0.005)
DCE 109	5.04 (0.60)	6.23 (0.69)	10.58 (1.21)	0.170 (0.027)
DCE 092	25.93 (1.06)	50.59 (1.68)	30.68 (0.86)	0.061 (0.003)
DCE 063	16.75 (2.30)	24.12 (1.10)	9.41 (1.34)	0.039 (0.006)

NOTE. — DCE 038 and DCE 090 column densities are not derived because their N_2H^+ 101-012 component is not detected (see text for details).

and

$$N_{\text{tot}}^{\text{thin}} = \frac{8\pi W}{\lambda^3 A} \frac{g_l}{g_u} \frac{1}{[J(T_{\text{ex}}) - J(T_{\text{bg}})]} \frac{1}{1 - \exp(-h\nu/kT_{\text{ex}})} \frac{Q_{\text{rot}}(T_{\text{ex}})}{g_l \exp(-E_l/kT_{\text{ex}})} \quad (3)$$

where τ is the total opacity of the multiplet, W is the total integrated intensity of the multiplet (scaled by the beam filling factor $\theta_{\text{size}}^2/(\theta_{\text{size}}^2 + \theta_{\text{beam}}^2)$, see §4.1), A is the Einstein coefficient, g_l and g_u are the statistical weights of the lower and upper levels, Q_{rot} is the rotational partition function under LTE conditions, and E_l is the energy of the lower level. The column densities are listed in Col. (3) and Col. (4) of Table 5 and the $\text{N}(\text{N}_2\text{D}^+)/\text{N}(\text{N}_2\text{H}^+)$ ratios are listed in Col. (5). The uncertainties reported in Col. 5 take into account the uncertainties on the measured integrated intensities but neglect the uncertainty on T_{ex} because it does not significantly affect the $\text{N}(\text{N}_2\text{D}^+)/\text{N}(\text{N}_2\text{H}^+)$ ratio. For a typical excitation temperature of ~ 5.4 K in our sample, the $\text{N}(\text{N}_2\text{D}^+)/\text{N}(\text{N}_2\text{H}^+)$ ratio will only increase by $\sim 7\%$ and decrease by $\sim 9\%$ if the excitation temperature increases by 1 K and decreases by 1 K, respectively. The effect is even smaller at a higher excitation temperature; the $\text{N}(\text{N}_2\text{D}^+)/\text{N}(\text{N}_2\text{H}^+)$ ratio will increase by $\sim 20\%$ if the excitation temperature increases by 5 K. Another noteworthy uncertainty could come from the unresolved hyperfine structure of $J = 3 \rightarrow 2$. We note also that the opacity correction applied in Eq. (2) slightly overestimates the column density because the total opacity of the multiplet, τ , is higher than the opacities of the individual components.

We also derive the N_2H^+ column densities from the $J = 1 \rightarrow 0$ transition with Eqs. (2) and (3), using only the 101-012 component that is not affected by other hyperfine components (see Col. (2) of Table 5). The N_2H^+ column densities derived from N_2H^+ (1–0) are slightly larger than that from RADEX (the best-fit models) by factors of 1.0 to 1.5 except for DCE 001 (0.6) and DCE 025 (0.9). The average of the factors is 1.2 with a standard deviation of 0.25. This result makes sense because LTE analysis will overestimate the N_2H^+ populations in $J > 1$ levels when the collision rate is insufficient to pump

N_2H^+ with low volume densities (non-LTE). The column densities derived from N_2H^+ (3–2) (Col. (3) of Table 5) are also larger than that from the RADEX best-fit model (Col. (4) of Table 4) by factors of 1.4 – 3.9, with an average value of 2.1 and a standard deviation of 0.6. The column densities of N_2D^+ listed in Col. (4) of Table 5 are thus likely overestimated by similar factors. However, as explained above, the $\text{N}_2\text{D}^+/\text{N}_2\text{H}^+$ column density ratios in Col. (5) should be reliable.

4.3. Asymmetry parameters

To probe the infall motion of our target cores, we used the asymmetry parameter defined by Mardones et al. (1997),

$$\delta v = \frac{v_{\text{thick}} - v_{\text{thin}}}{\Delta v_{\text{thin}}}, \quad (4)$$

where v_{thick} and v_{thin} are the velocities of the optically thick line and optically thin line, respectively, and Δv_{thin} is the line width of the optically thin line. We used N_2H^+ (1–0) as our optically thin tracer, and v_{thin} and Δv_{thin} are derived from HFS fitting (Table 2). The HFS fitting provides the line width that corresponds to the width of the opacity profile. It should represent the velocity dispersion well and can thus be used as a proxy for Δv_{thin} . Eleven out of our sixteen sources have optical depths lower than 1.3 for the strongest hyperfine component (123–012, $\tau_{\text{tot}} \times 7/27$), suggesting that the systemic velocity derived from the HFS fitting should not be significantly affected by optical depth effects and can be used as a proxy for v_{thin} . For the remaining sources, three (DCE 081, 185, and 092) have optical depths lower than 1.3 for the isolated hyperfine component (101–012, $\tau_{\text{tot}} \times 3/27$). The systemic velocity derived from the HFS fitting matches well the centroid velocity of the isolated component for these three sources and can thus also be used as a proxy for v_{thin} . For DCE 182, although the N_2H^+ (1–0) emission is very weak and the opacity is not constrained, its emission is most likely optically thin. The remaining source, DCE 004, is optically thin ($\tau \sim 0.5$) in the faintest hyperfine component (110–011, $\tau_{\text{tot}} \times 1/27$). In this source, this component is well separated from the other hyperfine components and a simple Gaussian fitting yields a systemic velocity consistent with the one derived from the HFS fitting. HCO^+ (3–2) and HCN (3–2) are used as optically thick tracers. v_{thick} corresponds to the peak velocity and we assume a 2σ uncertainty of 0.14 km s^{-1} , which is equal to half of the channel width. The asymmetry parameters calculated from HCO^+ (3–2) and HCN (3–2) are listed in Table 6.

We use $|\delta v| \geq 3\sigma_{\delta v}$ ($\text{S/N} \geq 3$) to define the significant detections of blueshifts (infall motion) or redshifts (outward motion). These sources are separated into three groups, which are 1) $\delta v \leq -3\sigma_{\delta v}$: clear indication of infall, 2) $\delta v \geq 3\sigma_{\delta v}$: redshifted optically thick line, and 3) $3\sigma_{\delta v} > \delta v > -3\sigma_{\delta v}$: no clear indication of systematic motion. With the numbers of sources in the three groups, we calculated the blue excess defined by Mardones et al. (1997),

$$\text{blue excess} = \frac{N_{\text{blue}} - N_{\text{red}}}{N_{\text{total}}}, \quad (5)$$

to study the statistical properties of our LLO sample.

TABLE 6
INFALL SIGNATURES

Source	δv			V_{in}
	HCO^+	HCN	consistency	[km s^{-1}]
DCE065	-0.06 (0.15)	-0.34 (0.16)	YES	0.73 (0.17)
DCE004	-0.78 (0.24)	-1.23 (0.25)	YES	0.14 (0.02)
DCE064	-0.80 (0.20)	-0.37 (0.20)	YES	-0.62 (0.15)
DCE031	0.53 (0.14)	0.63 (0.14)	YES	-
DCE001	-0.36 (0.12)	-0.57 (0.12)	YES	0.07 (0.03)
DCE181	0.43 (0.28)	-	-	-
DCE081	0.82 (0.18)	-0.21 (0.18)	NO	-0.13 (0.03)
DCE025	1.32 (0.20)	1.43 (0.20)	YES	-0.08 (0.04)
DCE038	-0.39 (0.18)	-	-	0.41 (0.18)
DCE185	1.31 (0.31)	-1.00 (0.31)	NO	-
DCE109	0.16 (0.16)	-0.13 (0.16)	NO	-1.04 (0.15)
DCE092	-0.39 (0.11)	-0.59 (0.11)	YES	0.58 (0.06)
DCE182	-0.58 (0.23)	-	-	0.59 (0.29)
DCE107	0.36 (0.13)	0.15 (0.12)	YES	-0.46 (0.08)
DCE063	-0.03 (0.11)	0.20 (0.11)	NO	0.72 (0.22)
DCE090	-0.08 (0.25)	-0.54 (0.26)	YES	0.26 (0.05)

NOTE. — The values in parenthesis represent 1σ uncertainties.

The blue excess is 0.07 (excluding DCE 185, see below) and 0.15 for HCO^+ (3–2) and HCN (3–2), respectively. These results are not very different from that the results of previous works, *i.e.* 0.25 from Mardones et al. (1997), 0.28 from Gregersen et al. (2000) and 0.05 from Emprechtinger et al. (2009). We also use the binomial test to determine if the number of blueshifted sources is significant (Rygl et al. 2013). The survival functions are 0.50 for HCO^+ (3–2) and 0.34 for HCN (3–2), suggesting that the number of blueshifted detections is not significant in our sample for both HCO^+ (3–2) and HCN (3–2).

4.4. Two-layer model fitting

We fitted the HCO^+ (3–2) spectra with the two-layer model (Myers et al. 1996) to derive the infall velocities of our targets. We used a simple version defined by Lee et al. (2001)

$$T_{MB} = J(T_r)(1 - e^{-\tau_r})e^{-\tau_f} + J(T_{\text{bg}})(e^{-\tau_f - \tau_r} - e^{-\tau_f}), \quad (6)$$

where T_{bg} is the cosmic background temperature (2.73 K), T_r is the excitation temperature of the rear layer, and τ_f and τ_r are the optical depths of the front and rear layers, respectively. The optical depths are expressed as $\tau_f = \tau_0 \exp[-(v - V_f)^2/2\sigma^2]$ and $\tau_r = \tau_0 \exp[-(v + V_r)^2/2\sigma^2]$, where τ_0 is the peak optical depth, V_f and V_r are the systemic velocities of the front and rear layers, respectively, and σ is the velocity dispersion. Considering the relative velocity of the two layers as the infall velocity (*i.e.* $V_f = V_r = V_{\text{in}}/2$), we fitted the spectra with eq. (6) to obtain the infall velocities (Figure 2). A positive infall velocity represents an inward motion in the core while a negative one indicates an outward motion. The spectral resolution (0.28 km s^{-1}) is sometimes insufficient to resolve the double-peak features and/or asymmetry structures. We therefore only list the fitting results with infall or outward velocities above the uncertainties (Table 6). As a result, the infall velocities are positive in 8 sources, negative in 5 sources and unconstrained in 3 sources.

5. DISCUSSION

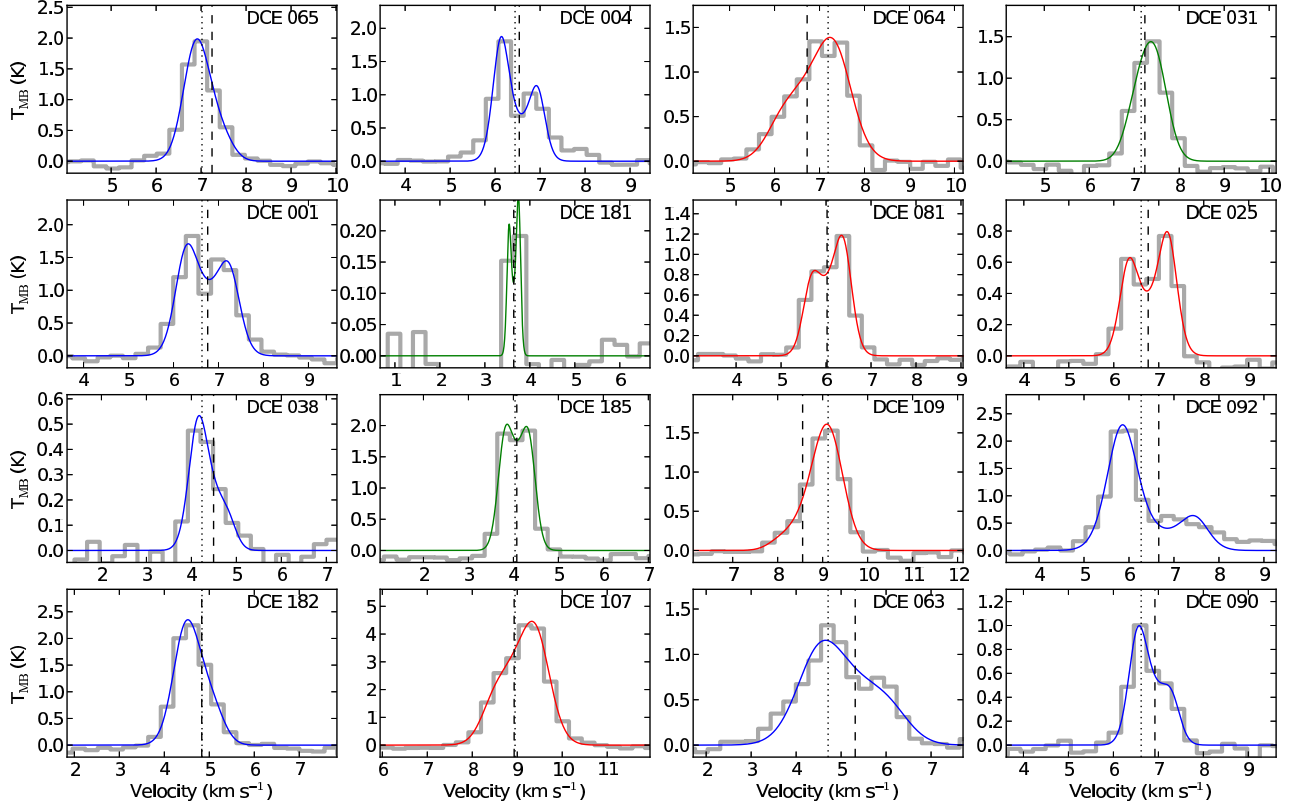


FIG. 2.— Two-layer radiative transfer model fits to the HCO^+ (3–2) spectra for the 16 targets. The fitting results are shown in blue line for $V_{\text{in}} > 0$, red line for $V_{\text{in}} < 0$ and green for unconstrained V_{in} . The vertical dashed line indicates the V_{LSR} from the two-layer model fitting and the vertical dotted line indicates the V_{LSR} from the N_2H^+ hyperfine fitting.

5.1. The physical conditions from Non-LTE RADEX analysis

Table 4 shows the physical parameters derived with RADEX. The kinetic temperature (T_{kin}), N_2H^+ column density ($N(\text{N}_2\text{H}^+)$), H_2 density (n_{H_2}) and source sizes of five cores are constrained in the RADEX analysis. Eight sources have no constraints in their kinetic temperatures and H_2 densities; the data are unable to discriminate models between a wide variety. Additional spectral lines or higher angular resolution data would be required to discriminate the models for these sources. Data with higher sensitivity could also break the degeneracy (see Appendix). The variances of T_{kin} and n_{H_2} from the fitting models are always anti-correlated; the fitting-models can either have high T_{kin} with low n_{H_2} or low T_{kin} with high n_{H_2} . With the currently available data, we discuss the physical properties with the best-fit models from both the 5 constrained sources and the 8 unconstrained sources. Our LLO targets have T_{kin} in a range between 5.0 K and 33 K, and a median of 8.0 K. (The corresponding thermal line widths are 0.09, 0.24 and 0.12 km s^{-1} for N_2H^+ .) The H_2 densities are populated in a range between 10^5 cm^{-3} and $2 \times 10^6 \text{ cm}^{-3}$ with a median of $4 \times 10^5 \text{ cm}^{-3}$ (excluding DCE 001 and 185 which have uniquely high $n_{\text{H}_2} = 2 \times 10^7 \text{ cm}^{-3}$ in our sample, see §4.1). Comparing with the Class 0 sample ($T_{\text{kin}} = 9 - 15 \text{ K}$ and $n_{\text{H}_2} = 5 \times 10^6 - 10^7 \text{ cm}^{-3}$) from Emprechtinger et al. (2009), LLOs have relatively lower n_{H_2} and a wider T_{kin} distribution; the standard deviation of T_{kin} for our LLO

sample is ~ 9.3 which is much larger than that of the Class 0 sample, ~ 1.7 . The derived H_2 densities of LLOs also spread in a larger range (~ 1.3 magnitude) than the Class 0 objects even after excluding DCE 001 and 185. We think this result comes from a wide variety of natures of our LLO targets which include some Class I objects and are located in different molecular clouds or isolated cores while the Class 0 sources in Emprechtinger et al. (2009) are all in the Perseus molecular cloud. Note that Emprechtinger et al. (2009) derived n_{H_2} using N_2D^+ (2–1) and (3–2) lines, and the kinetic temperatures were derived by Hatchell (2003) and Jijina et al. (1999) with NH_3 lines.

A caveat in the H_2 density comparison is that the beam size of our data is much larger than that from Emprechtinger et al. (2009). The larger beam could make the derived H_2 density lower if it is diluted by a large area. To fairly compare the H_2 densities, we scale our derived n_{H_2} to the observing beam size of N_2D^+ (2–1) ($16.3''$) from Emprechtinger et al. (2009). Assuming a density profile, $\rho(r) \propto r^{-2}$, we calculate an average density, $\rho_{\text{ave}}(<r) \propto r^{-2}$, within a radius r . We can therefore obtain an expected H_2 density within $16.3''$ area based on our derived H_2 density and source size. The scaled H_2 density is populated in a range between $7 \times 10^4 \text{ cm}^{-3}$ and $3 \times 10^7 \text{ cm}^{-3}$ with a median of $2 \times 10^6 \text{ cm}^{-3}$. Our derived H_2 densities therefore have a wider distribution compared with the Class 0 sample. Excluding DCE 001 and 185 (see §4.1), 3 LLOs have H_2 density higher than Class 0 sources and 8 have lower H_2 density. There-

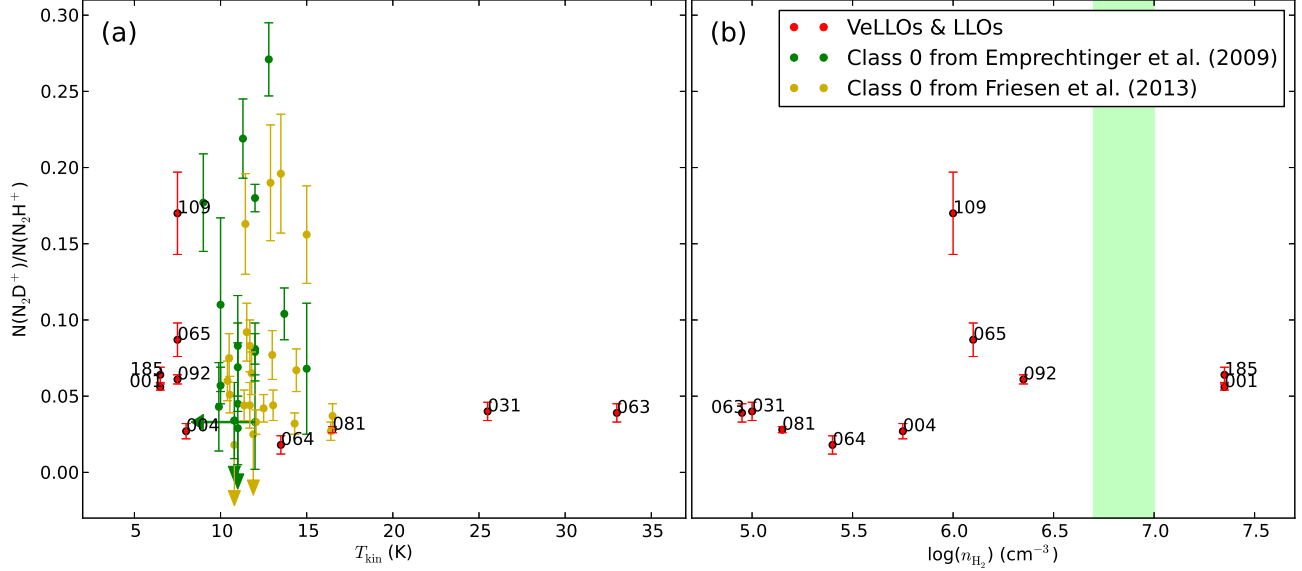


FIG. 3.— Comparison of N_2D^+/N_2H^+ column density ratio with T_{kin} and n_{H_2} . The Class 0 data are from Emprechtinger et al. (2009) (green) and Friesen et al. (2013) (yellow). The error bar indicates 1σ uncertainty in our data (red). The green area represents the range of H_2 densities of the Class 0 objects from Emprechtinger et al. (2009).

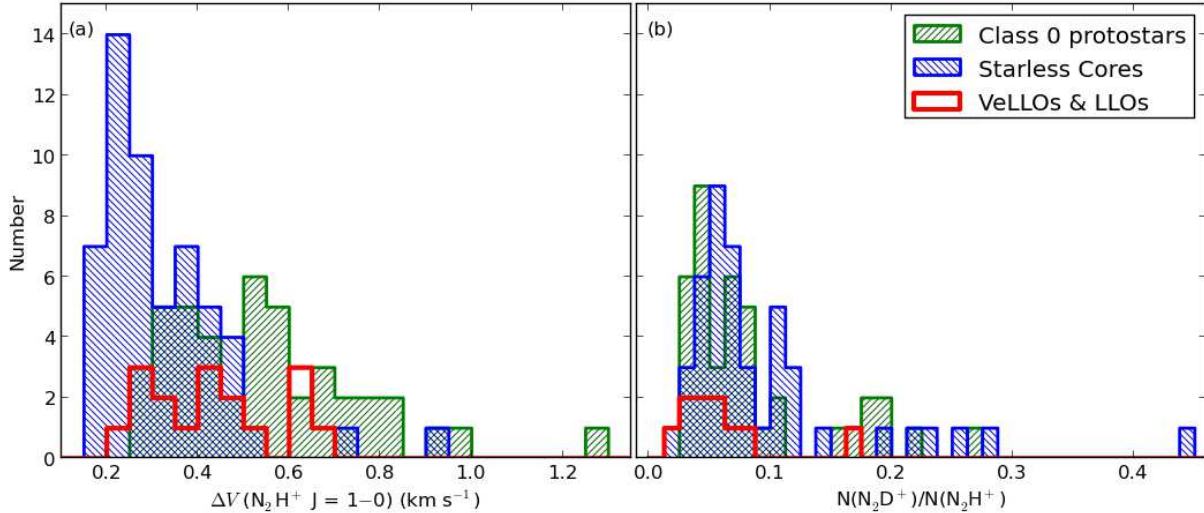


FIG. 4.— Populations of line width (a) and N_2D^+/N_2H^+ column density ratio (b) for Class 0 protostars (green), Starless cores (blue) and LLOs (red). The Class 0 protostar and starless core data are from Emprechtinger et al. (2009), Friesen et al. (2013) and Crapsi et al. (2005b).

fore, LLOs are likely to have relatively low H_2 densities compared with Class 0 sources after correcting for the different beam sizes.

5.2. $N(N_2D^+)/N(N_2H^+)$ ratio as an age indicator

To investigate the relation between chemistry and physical conditions in these cores, we compare the $N(N_2D^+)/N(N_2H^+)$ ratio with the derived kinetic temperature (or gas temperature) and H_2 density (Figure 3). Figure 3a includes the Class 0 objects from Emprechtinger et al. (2009) and Friesen et al. (2013). The kinetic temperatures are derived using $N_2H^+ J = 3-2/J = 1-0$ in our study, and using $NH_3 (1, 1)/(2, 2)$ in Emprechtinger et al. (2009) and Friesen et al. (2013). The sources with the highest $N(N_2D^+)/N(N_2H^+)$ ratios

(> 0.05) all have low kinetic temperatures (< 10 K). We use Pearson's r correlation test and Spearman's ρ rank correlation test (Conover et al. 1999) to evaluate the significances of correlations between $N(N_2D^+)/N(N_2H^+)$ ratios and kinetic temperatures for our LLO sample. The Pearson correlation coefficient, $r \sim -0.38$ with a significance of 0.28, provides no evidence of (linear) correlation between T_{kin} and $N(N_2D^+)/N(N_2H^+)$ ratio. However, the Spearman rank correlation coefficient, $\rho \sim -0.61$ with a significance of 0.06 (the probability for this sample to be an uncorrelated system), implies an existence of anti-correlation. This features are predicted by chemical models; the $N(N_2D^+)/N(N_2H^+)$ ratio is expected to increase in cold regions. However, we did not find any significant correlation between the $N(N_2D^+)/N(N_2H^+)$

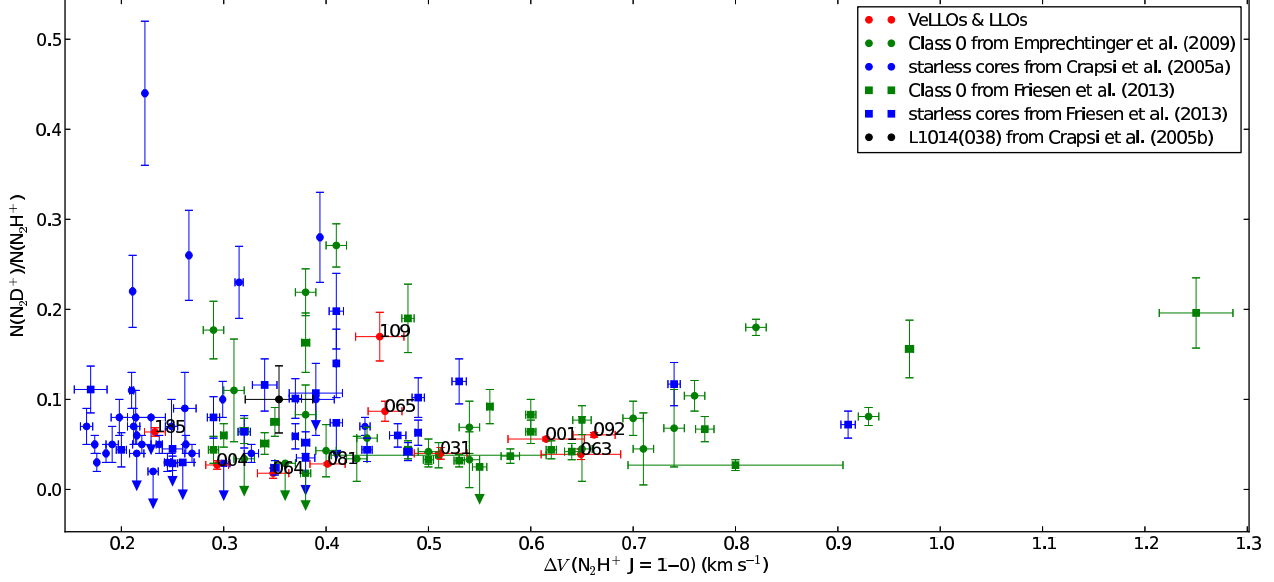


FIG. 5.— Line widths of N_2H^+ (1–0) versus $\text{N}(\text{N}_2\text{D}^+)/\text{N}(\text{N}_2\text{H}^+)$ ratios. The colors represent the different type of sources as Fig. 2. The error bars indicate 1σ uncertainties in our data (red).

ratio and n_{H_2} (Figure 3b).

To study the evolutionary states of LLOs, we compare the chemical evolutionary indicator, $\text{N}(\text{N}_2\text{D}^+)/\text{N}(\text{N}_2\text{H}^+)$ ratio, and the dynamical evolutionary indicator, N_2H^+ (1–0) line width, with that of starless cores and Class 0 sources from Crapsi et al. (2005b), Emprechtinger et al. (2009) and Friesen et al. (2013). Figures 4a and 4b show the line width and $\text{N}(\text{N}_2\text{D}^+)/\text{N}(\text{N}_2\text{H}^+)$ ratio populations, respectively. The line widths of Class 0 sources are relatively larger than that of starless cores, and most of our LLOs are located in the region where Class 0 sources and starless cores overlap (Figure 4a). This result implies that LLOs are likely young Class 0 sources whereas there is no significant difference in their $\text{N}(\text{N}_2\text{D}^+)/\text{N}(\text{N}_2\text{H}^+)$ ratio (Figure 5). The $\text{N}(\text{N}_2\text{D}^+)/\text{N}(\text{N}_2\text{H}^+)$ ratios (median=0.05) of our LLOs are similar to that of starless cores and Class 0 sources, although only 10 sources have N_2D^+ (3–2) detections. (Though N_2D^+ $J = 3 \rightarrow 2$ is detected in DCE 107, the two components are unresolvable, which prevents us from deriving the N_2D^+ column density for each component.)

5.3. Infall indicators

Figure 6 shows the comparison of the asymmetry parameters calculated from HCO^+ (3–2) and HCN (3–2). The asymmetry parameters obtained from HCO^+ (3–2) and HCN (3–2) are quite consistent with each other except for DCE 185; HCO^+ (3–2) δv and HCN (3–2) δv show a positive correlation. For the 13 targets with both HCO^+ (3–2) and HCN (3–2) detections, 9 targets have the same mathematical sign (Table 6). The remaining 4 sources are DCE 081, 185, 109 and 063. The asymmetry parameters of DCE 109 and 063 have S/N ratios less than 2σ for both HCO^+ (3–2) and HCN (3–2), which implies that no clear systematic motions are occurring (Figure 6). The HCO^+ (3–2) spectrum of DCE 185 shows a double-peak profile and the peak values are very similar.

If we used the alternative peak, the asymmetry parameter would become -1.12, which would be consistent to that from HCN (3–2). However, it is still unclear if DCE 185 has a clear infall or redshifted signature based on the low spectral resolution data. The DCE 081’s HCN (3–2) δv indicates no clear systematic motion ($\sim 1.2\sigma$) and its HCN (3–2) detection is quite weak ($\text{S/N} \sim 4.2$). Since its HCO^+ (3–2) spectrum shows clear asymmetry profile (see below), we suggest that its asymmetry parameter from HCO^+ (3–2) is much more reliable than that from HCN (3–2) for DCE 081.

Using the two-layer model, the infall velocities of 13 targets are derived using the HCO^+ (3–2) spectra. We compared the derived infall velocities with previous works. Belloche et al. (2002) have derived an infall velocity field in DCE 001 (IRAM 04191). The infall velocity is decreasing from the center and becomes uniform ($V_{\text{in}} \sim 0.10 \pm 0.05 \text{ km s}^{-1}$) between ~ 2000 – 3000 AU and ~ 10000 – 12000 AU . Our derived infall velocity, $0.07 \pm 0.03 \text{ km s}^{-1}$, is consistent with this infall velocity field in the outer region. For DCE 004 (L1521F), our derived infall velocity 0.14 ± 0.02 is slightly smaller than the infall velocity 0.2 – 0.3 km s^{-1} (2000 to 3000 AU) from Onishi et al. (1999), but much larger than that from Lee et al. (2004), 0.014 km s^{-1} and 0.045 km s^{-1} from CS (2–1) and (3–2) spectra, respectively. Lee et al. (2004) concluded that the CS (2–1) and (3–2) may trace different regions, which results in a difference between the derived infall velocities. HCO^+ (3–2) may trace a more excited region since it has a higher energy level. In addition, the difference of optical depth and depletion between molecules may also explain the discrepancy between infall velocity measurements.

We also compared the infall velocities with the free-fall velocities. The free-fall velocities, $v_{\text{ff}} = (GM/R)^{1/2}$ (Keto et al. 2004) where M and R are the envelope mass and radius, respectively, are derived from the RADEX best-fit models assuming the central star has a negligible

mass. All sources have infall velocities less than free-fall velocities except for DCE 038, 063 and 090. The infall velocities of these three sources are not significantly larger than their free-free fall velocities (within 3σ uncertainty of V_{in}). Thus, none of our targets has infall velocity significantly larger than its free-fall velocity.

All the sources with positive V_{in} have negative HCO^+ (3–2) δv and vice versa except for DCE 064. This result suggests that the infall or red shifted (outward) signatures are quite reliable in the HCO^+ infall analysis. For DCE 064, the asymmetry spectrum with blueshifted wing suggesting an expanding motion is in contrast to the negative δv derived from both HCO^+ (3–2) and HCN (3–2). The spectral resolution of our current data is insufficient to identify if DCE 064 has an infalling or expanding envelope. We find that the HCO^+ spectrum of DCE 064 has a double-peak profile, and the peak values are similar as DCE 185. The HCO^+ δv will be ~ 0.8 (expanding) if we use the second peak whereas the δv derived from the first peak is -0.78 . In addition, the asymmetry parameter of HCN (3–2), $\delta v = -0.37$, is not significant ($S/N \sim 1.8$). Therefore, the blue shifted wing hints that outward motion may occur in DCE 064.

It is noteworthy that the HCO^+ systemic velocities from the two-layer model fitting are occasionally shifted from the systemic velocities obtained from N_2H^+ (Figure 2). These results suggest that HCO^+ and N_2H^+ trace different regions in the cores, and hint that the derived asymmetry parameters could be false. Observations of optically thin isotopologue H^{13}CO^+ or HC^{18}O^+ are required to correct the infall measurements by providing an unbiased V_{LSR} . HCO^+ can also trace the protostellar outflows which could contaminate our determinations of infall motions. Besides, more complicated dynamic structures such as molecular outflows or core rotation could affect our results. In addition, Smith et al. (2012) found that the blue asymmetry parameters could be frequently undetected toward collapsing cores located in filaments. Based on radiative transfer models, Smith et al. (2012) found that geometry parameters such as inclination angle will significantly affect the profile of optically thick tracers like CS (2–1) and HCN (1–0). In order to find a reliable infall indicator, Chira et al. (2014) modeled the line profiles of HCO^+ and HCN among transitions from $J = 1 \rightarrow 0$ to $J = 5 \rightarrow 4$. They found that $J = 4 \rightarrow 3$ has the best chance to probe infall motions, but the $J = 3 \rightarrow 2$ and $J = 5 \rightarrow 4$ transitions of both HCN and HCO^+ are also good indicators.

As a result, 8 sources have positive infall velocities (infall motions) and 5 sources have negative infall velocities (outward motions). Out of the 8 infall candidates, 3 sources (DCE 004, 001, and 092) have significant blue asymmetry ($S/N \geq 3$) from both HCO^+ (3–2) and HCN (3–2). These 3 sources have very low kinetic temperatures ($6.5 \text{ K} < T_{\text{kin}} < 8.0 \text{ K}$) and bolometric temperatures ($20 \text{ K} < T_{\text{bol}} < 27 \text{ K}$). Four sources (DCE 065, 038, 182, and 090) have a blue asymmetry parameter in either HCO^+ (3–2) or HCN (3–2) in the range 2–3 σ , which suggests that infall motions may be occurring in these candidates too. DCE 065 and 038 also have low kinetic temperatures (7.5 and 9.0 K) and bolometric temperatures (29 and 66 K). DCE 182 and 090 have relatively high bolometric temperatures (105 and 114K, *i.e.* young

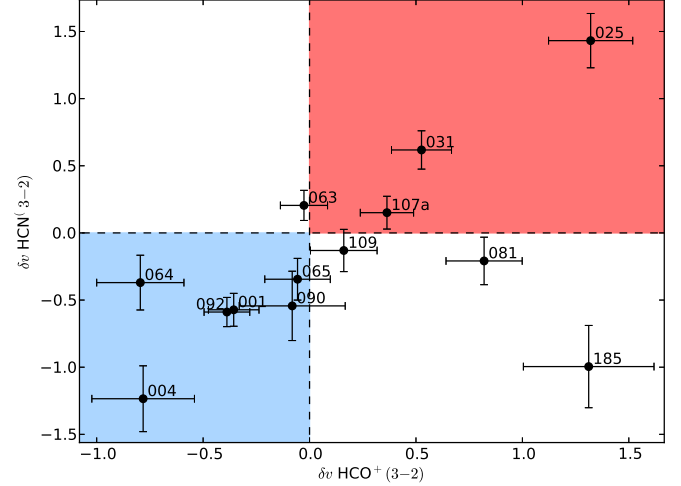


FIG. 6.— Asymmetry parameters derived from HCO^+ (3–2) versus that from HCN (3–2). The blue and red colors indicate the area for infall motion and outward motion, respectively. The error bars indicate 1σ uncertainties.

Class I sources), and DCE 090 has a high kinetic temperature of 30.5 K (T_{kin} of DCE 182 cannot be solved due to lack of N_2H^+ (3–2)). Our results suggest that the infall motions are likely to occur at an early evolutionary stage but can still appear at a later stage (Class I), which is consistent with Gregersen et al. (2000).

6. CONCLUSION

We observed N_2H^+ (1–0), N_2H^+ (3–2), N_2D^+ (3–2), HCO^+ (3–2) and HCN (3–2) toward 16 LLOs using the KP 12m telescope and SMT in ARO. We derived the kinetic temperatures, N_2H^+ column densities, H_2 densities and core sizes by fitting spectra with the non-LTE code RADEX. We obtain these physical parameters for 13 LLOs from N_2H^+ (1–0) and (3–2) observations. We derived the $N(\text{N}_2\text{D}^+)/N(\text{N}_2\text{H}^+)$ ratio which traces the evolutionary state of starless cores and protostellar cores. To further probe the infall motions, we used HCO^+ (3–2) and HCN (3–2) as optically thick tracers and N_2H^+ (1–0) as optically thin tracer. Our conclusions are the following:

1. LLOs tend to have relatively low H_2 densities compared with the Class 0 objects in Emprechtinger et al. (2009). Only DCE 001 and 185 have higher H_2 densities than Class 0 objects; however, their densities are most likely overestimated due to the beam size difference in N_2H^+ (1–0) and (3–2) observations.
2. For $T_{\text{kin}} < 10 \text{ K}$, LLOs have $\text{N}_2\text{D}^+/\text{N}_2\text{H}^+$ column density ratios between 0.03–0.17 similar to the Class 0 objects observed by Emprechtinger et al. (2009) and Friesen et al. (2013), and for $T_{\text{kin}} > 10 \text{ K}$, LLOs have consistently low $\text{N}_2\text{D}^+/\text{N}_2\text{H}^+$ column density ratios ~ 0.04 . The Spearman rank correlation test implies an anti-correlation between the $\text{N}_2\text{D}^+/\text{N}_2\text{H}^+$ column densities and the kinetic temperatures in LLOs with a significance of 0.06.
3. We find that the $\text{N}_2\text{D}^+/\text{N}_2\text{H}^+$ column density ratios of LLOs are similar to that of starless cores

and Class 0 objects, but the line widths of LLOs are mostly populated in the starless cores and Class 0 objects overlapping region. We suggest that the molecular line width could be a better age indicator than $N(N_2D^+)/N(N_2H^+)$ ratio at the early stage and LLOs are likely young Class 0 protostellar sources.

4. We identify eight infall candidates by fitting the HCO^+ (3–2) spectra with a two-layer model. Seven sources are supported by their asymmetry parameters with $S/N > 2$ in either or both HCO^+ (3–2) or HCN (3–2). Our result suggests that infall motions tend to occur at a very early evolutionary stage but

can still occur in young Class I sources (DCE 090 and 182).

T.H.H. and S.P.L. acknowledge support from the Ministry of Science and Technology (MOST) of Taiwan with Grants NSC 101-2119-M-007-004 and MOST 102-2119-M-007-004-MY3. T.H.H. thanks to MOST for granting him the PhD exchanging student award (MOST 103-2917-I-007-005) to visit MPIfR from Feb 2014 to Jan 2015, and is also indebted to Prof. Dr. Karl M. Menten for his visiting in MPIfR.

REFERENCES

- André, P., Motte, F., & Bacmann, A. 1999, *ApJ*, 513, L57
- André, P., Ward-Thompson, D., & Greaves, J. 2012, *Sci*, 337, 69
- Barsony, M., Wolf-Chase, G. A., Ciardi, D. R., & O’linger, J. 2010, *ApJ*, 720, 64
- Belloche, A., André, P., Despois, D., & Blinder, S. 2002, *A&A*, 393, 927
- Belloche, A., Parise, B., van der Tak, F. F. S., et al. 2006, *A&A*, 454, L51
- Belloche, A., Schuller, F., Parise, B., et al. 2011, *A&A*, 527, A145
- Bourke, T. L., Crapsi, A., Myers, P. C., et al. 2005, *ApJ*, 633, L129
- Bourke, T. L., Myers, P. C., Evans, N. J., II, et al. 2006, *ApJ*, 649, L37
- Caselli, P., Walmsley, C. M., Tafalla, M., Dore, L., & Myers, P. C. 1999, *ApJ*, 523, L165
- Caselli, P., Walmsley, C. M., Zucconi, A., et al. 2002, *ApJ*, 565, 344
- Caselli, P., & Ceccarelli, C. 2012, *A&ARv*, 20, 56
- Chen, H., Myers, P. C., Ladd, E. F., & Wood, D. O. S. 1995, *ApJ*, 445, 377
- Chen, X., Arce, H. G., Zhang, Q., et al. 2010, *ApJ*, 715, 1344
- Chen, X., Arce, H. G., Dunham, M. M., & Zhang, Q. 2012, *ApJ*, 747, L43
- Chen, X., Arce, H. G., Dunham, M. M., et al. 2012, *ApJ*, 751, 89
- Chira, R.-A., Smith, R. J., Klessen, R. S., Stutz, A. M., & Shetty, R. 2014, *MNRAS*, 444, 874
- Conover, W. J. 1999, *Practical Nonparametric Statistics* (3rd ed.; New York: Wiley), 271, 456
- Crapsi, A., DeVries, C. H., Huard, T. L., Lee, J.-E., et al. 2005a, *A&A*, 439, 1023
- Crapsi, A., Caselli, P., Walmsley, C. M., et al. 2005b, *ApJ*, 619, 379
- Crapsi, A., Caselli, P., Walmsley, C. M., et al. 2004, *A&A*, 420, 957
- Daniel, F., Dubernet, M.-L., Meuwly, M., Cernicharo, J., Pagani, L. 2005, *MNRAS*, 363, 1083
- Daniel, F., Cernicharo, J., & Dubernet, M.-L. 2006, *ApJ*, 648, 461
- Daniel, F., Cernicharo, J., Roueff, E., Gerin, M., & Dubernet, M.-L. 2007, *ApJ*, 667, 980
- Di Francesco, J., Evans, N. J., II, Caselli, P., et al. 2007, in *Protostars and Planets V*, ed. B. Reipurth, D. Jewitt, & K. Keil (Tucson: Univ. Arizona Press), 17
- Dore, L., Caselli, P., Beninatti, S., et al. 2004, *A&A*, 413, 1177
- Dullemond, C. P., & Dominik, C. 2004, *A&A*, 417, 159
- Dunham, M. M., Evans, N. J., II, Bourke, T. L., et al. 2006, *ApJ*, 651, 945
- Dunham, M. M., Crapsi, A., Evans, N. J., II, Bourke, T. L., Huard, T. L., Myers, P. C., & Kauffmann, J. 2008, *ApJS*, 179, 249
- Dunham, M. M., Evans, N. J., Bourke, T. L., et al. 2010a, *ApJ*, 721, 995
- Dunham, M. M., Evans, N. J., II, Terebey, S., Dullemond, C. P., & Young, C. H. 2010b, *ApJ*, 710, 470
- Dunham, M. M., Chen, X., Arce, H., et al. 2011, *ApJ*, 742, 1
- Dunham, M. M., & Vorobyov, E. I. 2012, *ApJ*, 747, 52
- Dunham, M. M., Stutz, A. M., Allen, L. E., et al. 2014, *arXiv:1401.1809*
- Emprechtinger, M., Caselli, P., Volgenau, N. H., Stutzki, J., & Wiedner, M. C. 2009, *A&A*, 493, 89
- Evans, N. J., II, Allen, L. E., Blake, G. A., et al. 2003, *PASP*, 115, 965
- Evans, N. J., II, Dunham, M. M., Jørgensen, J. K., et al. 2009, *ApJS*, 181, 321
- Enoch, M. L., Evans, N. J., II, Sargent, A. I., et al. 2008, *ApJ*, 684, 1240
- Enoch, M. L., Lee, J.-E., Harvey, P., Dunham, M. M., & Schnee, S. 2010, *ApJ*, 722, L33
- Friesen, R. K., Kirk, H. M., & Shirley, Y. L. 2013, *ApJ*, 765, 59
- Gegersen, E. M., Evans, N. J., II, Mardones, D., & Myers, P. C. 2000, *ApJ*, 533, 440
- Hatchell, J. 2003, *A&A*, 403, L25
- Huang, Y.-H., & Hirano, N. 2013, *ApJ*, 766, 131
- Huard, T. L., Myers, C. M., Murphy, D. C., et al. 2006, *ApJ*, 640, 391
- Hsieh, T.-H., & Lai, S.-P. 2013, *ApJS*, 205, 5
- Jijina, J., Myers, P. C., & Adams, F. C. 1999, *ApJS*, 125, 161
- Johnstone, D., Rosolowsky, E., Tafalla, M., & Kirk, H. 2010, *ApJ*, 711, 655
- Kauffmann, J., Bertoldi, F., Bourke, T. L., et al. 2011, *MNRAS*, 416, 2341
- Keto, E., Rybicki, G. B., Bergin, E. A., & Plume, R. 2004, *ApJ*, 613, 355
- Kenyon, S. J., Hartmann, L. W., Strom, K. M., & Strom, S. E. 1990, *AJ*, 99, 3
- Kim, H. J., Evans, N. J., II, Dunham, M. M., et al. 2011, *ApJ*, 729, 84
- Kirk, H., Johnstone, D., & Tafalla, M. 2007, *ApJ*, 668, 1042
- Larson, R. B. 1969, *MNRAS*, 145, 271
- Lee, C. W., Myers, P. C., & Tafalla, M. 2001, *ApJS*, 136, 703
- Lee, C. W., Bourke, T. L., Myers, P. C., et al. 2009, *ApJ*, 693, 1290
- Lee, C. W., Myers, P. C., & Plume, R. 2004, *ApJS*, 153, 523
- Lee, C. W., Kim, M.-R., Kim, G., et al. 2013, *ApJ*, 777, 50
- Lee, J.-E., Lee, H.-G., Shinn, J.-H., et al. 2010, *ApJ*, 709, L74
- Mangum, J., & Shirley, Y. 20013, <https://safe.nrao.edu/wiki/pub/Main/MolInfo/ColumnDensityCalculation-MangumShirley.pdf>
- Mardones, D., Myers, P. C., Tafalla, M., et al. 1997, *ApJ*, 489, 719
- Miettinen, O., & Offner, S. S. R. 2013, *A&A*, 555, A41
- Murillo, N. M., & Lai, S.-P. 2013, *ApJ*, 764, L15
- Myers, P. C., Mardones, D., Tafalla, M., Williams, J. P., & Wilner, D. J. 1996, *ApJ*, 465, L133
- Onishi, T., Mizuno, A., & Fukui, Y. 1999, *PASJ*, 51, 257
- Padoan, P., & Nordlund, Å. 2004, *ApJ*, 617, 559
- Pezzuto, S., Elia, D., Schisano, E., et al. 2012, *A&A*, 547, A54
- Pineda, J. E., Arce, H. G., Schenée, S., et al. 2011, *ApJ*, 743, 201
- Palau, A., Zapata, L. A., Rodríguez, L. F., et al. 2014, *MNRAS*, 444, 833
- Press, W. H., Teukolsky, S. A., Vetterling, W. T., & Flannery, B. P. 1992, *Numerical Recipes in C: The Art of Scientific Computing* (2nd ed.; Cambridge: Cambridge Univ. Press)
- Ridge, N. A., Francesco, J. D., Kirk, H., et al. 2006, *AJ*, 131, 2921
- Roberts, H., & Millar, T. J. 2007, *A&A*, 471, 849
- Rygl, K. L. J., Wyrowski, F., Schuller, F., & Menten, K. M. 2013, *A&A*, 549, A5
- Smith, R. J., Shetty, R., Stutz, A. M., & Klessen, R. S. 2012, *ApJ*, 750, 64
- Schöier, F. L., van der Tak, F. F. S., van Dishoeck, E. F., Black, J. H. 2005, *A&A*, 432, 369
- Tafalla, M., Myers, P. C., Caselli, P., & Walmsley, C. M. 2004, *A&A*, 416, 191
- Tafalla, M., Myers, P. C., Caselli, P., Walmsley, C. M., & Comito, C. 2002, *ApJ*, 569, 815
- Takahashi, S., Ohashi, Nagayoshi, & Bourke, T. L. 2013, *ApJ*, 774, 20
- Tsitali, A. E., Belloche, A., Commerçon, B., & Menten, K. M. 2013, *A&A*, 557, A98
- Tobin, J. J., Hartman, L., Bergin, E., Chiang, H.-F., et al. 2012, *ApJ*, 748, 16

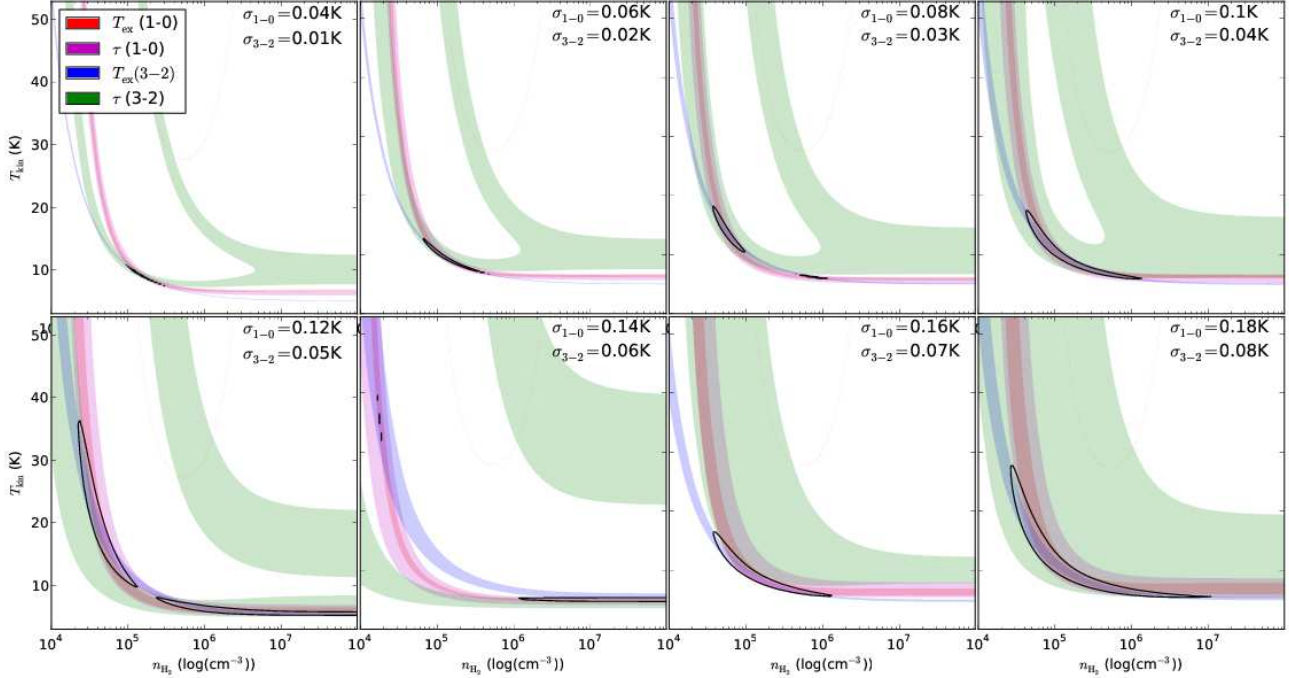


FIG. A1.— The slice in the model grid for T_{kin} versus n_{H_2} . The black line indicates the confidence interval which fits to the synthetic spectra. The color area indicates the models fit to the observing parameters, T_{ex} and τ , within their errors.

van der Tak, F. F. S., Black, J. H., Schöier, F. L., Jansen, D. J., & van Dishoeck, E. F. 2007, *ApJ*, 468, 627

Young, C. H., Jørgensen, J. K., Shirley, Y. L., et al. 2004, *ApJS*, 154, 396

APPENDIX

We evaluated the feasibility of using N_2H^+ (1–0) and (3–2) data to well constrain the physical parameters with RADEX. The method is to find the relation between the uncertainties of T_{kin} and n_{H_2} and a set of synthetic spectra with different rms noise levels. We first construct a reference model using RADEX and compute the synthetic N_2H^+ (1–0) and (3–2) spectra for this reference model. Then we added artificial noise to the spectra and derived the excitation temperatures and optical depths using the HFS fitting method. The data with lower rms noise levels would have lower uncertainties in their excitation temperatures and optical depths. We made grid of models with varied kinetic temperatures, H_2 densities, and N_2H^+ column densities. Then we compute the χ^2 for the reference model and each model in the grid based on the excitation temperatures and optical depths.

Here we describe the process and results in detail. Using RADEX without hyperfine structure, we derive T_{ex} and τ for both N_2H^+ (1–0) and (3–2) from a reference model set, $T_{\text{kin}} = 8.75$ K, $\log(n_{\text{H}_2}) = 5.225$, $N(\text{N}_2\text{H}^+) = 1.1 \times 10^{13} \text{ cm}^{-2}$ and core size = $75''$. We constructed the synthetic N_2H^+ (1–0) and (3–2) spectra with

$$T_{\text{MB}}(v) = \Psi(J(T_{\text{ex}}) - J(T_{\text{bg}}))(1 - \exp(-\tau(v))), \quad (1)$$

considering the beam sizes of $67.5''$ for N_2H^+ (1–0) and $27''$ for N_2H^+ (3–2). We added noise into the synthetic spectra. The noise levels are from 0.04 to 0.16 K (at a spectral resolution of 0.078 km s^{-1}) with a step of 0.02 K for N_2H^+ (1–0) and from 0.01 to 0.07 K (at a spectral resolution 0.27 km s^{-1}) with a step of 0.01 K for N_2H^+ (3–2); in total, seven sets of synthetic spectra are constructed. (The rms noise level of our observational data are ~ 0.1 K and ~ 0.04 K for these two transitions.) We obtain T_{ex} and τ using HFS fits to the synthetic spectra. As expected, the errors of T_{ex} and τ are correlated to the artificial rms noise levels. We then construct a grid of models with varied kinetic temperatures, H_2 densities, and N_2H^+ column densities. We calculate the $\Delta\chi^2$ using the T_{ex} and τ from the synthetic spectra of the reference model and that from each model in the grid, *i.e.* $\Delta\chi^2 = \left(\frac{T_{\text{ex},1-0} - T_{\text{ex},1-0,\text{model}}}{\sigma_{T_{\text{ex},1-0}}}\right)^2 + \left(\frac{\tau_{1-0} - \tau_{1-0,\text{model}}}{\sigma_{\tau_{1-0}}}\right)^2 + \left(\frac{T_{\text{ex},3-2} - T_{\text{ex},3-2,\text{model}}}{\sigma_{T_{\text{ex},3-2}}}\right)^2 + \left(\frac{\tau_{3-2} - \tau_{3-2,\text{model}}}{\sigma_{\tau_{3-2}}}\right)^2$. Figure A1 shows the 68.3% confidence interval in the slices of T_{kin} vs. n_{H_2} space. The color regions represent the models fitting the observing parameters within the errors. The regions become broader when the uncertainties become larger with larger rms noise levels. With a fixed T_{ex} or τ , the fitting models are always populated from high T_{kin} with low n_{H_2} to low T_{kin} with high n_{H_2} . This phenomenon explains that the models with high T_{kin} low n_{H_2} , and low T_{kin} high n_{H_2} are sometimes discriminated with difficulty. As a result, we provided the reference values of noise for deriving the physical parameters. For example, the data set with best sensitivity, $\sigma_{1-0} \sim 0.04$ K and $\sigma_{3-2} \sim 0.01$ K, can be used to constrain the T_{kin} in a range of ~ 7 –11 K and the n_{H_2} in a range of $\sim 6.3 \times 10^4$ – $1.6 \times 10^5 \text{ cm}^{-3}$ (Figure A1). Note that if we fit the

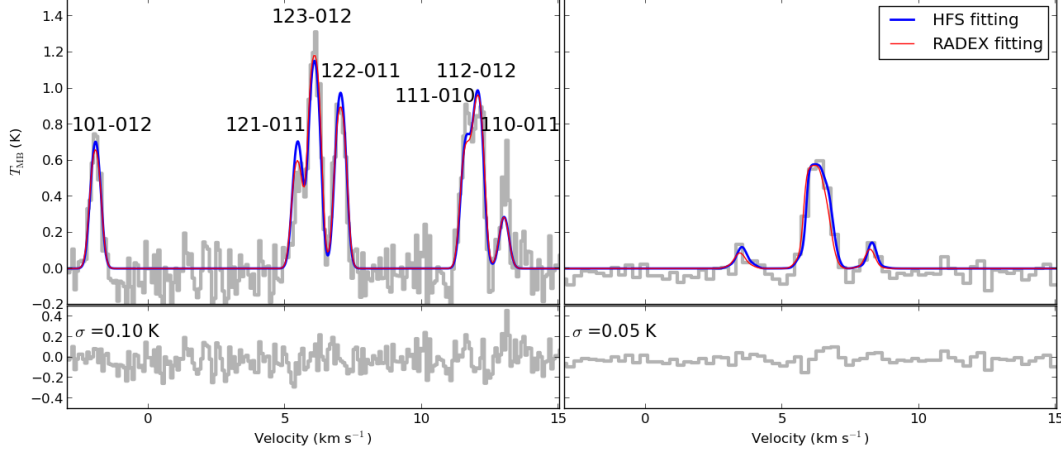


FIG. A2.— Comparison of HFS fitting (blue) and RADEX fitting (red) for DCE 081. The left and right panels show the N_2H^+ (1–0) and (3–2) spectra of DCE 081, respectively. The bottom panels show the residuals of the RADEX fit.

spectra with HSF directly, the degeneracy can be marginally reduced (see §4.1). Our analysis provides the reference sensitivity which is required for constraining the physical conditions with RADEX. However, the analysis does not guarantee that the sensitivity allows to achieve the constraint as our example. If the best-fit model is located in a different region, the confidence interval is expected to be different.